


Original Research

Dual-Modified Mannose/RVG29 Peptide-Functionalized Lipid Nanoparticles Loaded With *circHIPK2* siRNA Ameliorate Hypoxic–Ischemic Brain Damage in Neonatal Mice by Suppressing Astrocyte Activation

Yinxia Dang^{1,†}, Fuhui Shen^{1,†}, Shengxia Wang¹, Yating Zhang¹, Xia Lu¹, Dongyuan Qin¹, Dan Feng¹, Yanjun Song¹, Zihuan Cheng¹, Ruicong Ma¹, Fan Wang^{1,*} 

¹Department of Neonatology, Lanzhou University Second Hospital, 730030 Lanzhou, Gansu, China

*Correspondence: wangfan1018@sina.com (Fan Wang)

†These authors contributed equally.

Academic Editor: Hahn Young Kim

Submitted: 22 July 2025 Revised: 16 September 2025 Accepted: 16 October 2025 Published: 16 December 2025

Abstract

Background: To address the unmet need for targeted therapeutic strategies for neonatal hypoxic–ischemic encephalopathy (HIE), we developed a brain-targeting lipid nanoparticle delivery system capable of silencing circular RNA homeodomain-interacting protein kinase 2 (*circHIPK2*) in astrocytes and investigated its ability to mediate neuroinflammation and improve neurological outcomes. **Methods:** Dual-modified 1,2-distearoyl-sn-glycero-3-phosphoethanolamine-poly (ethylene glycol)-neurotropic virus-derived peptide (DSPE-PEG2000-RVG29) peptide/mannose-functionalized lipid nanoparticles loaded with *circHIPK2* small interfering RNA (M-R@siC-NPs) were constructed, and their physicochemical properties, stability, and biocompatibility were characterized. Using an *in vitro* oxygen-glucose deprivation (OGD) model and a neonatal murine hypoxic–ischemic brain damage (HIBD) model, we evaluated the effects of *circHIPK2* silencing by the M-R@siC-NPs on the expression of two astrocyte activation markers, glial fibrillary acidic protein (GFAP) and interleukin-1 β (IL-1 β), via western blotting, quantitative reverse transcription-polymerase chain reaction (qRT-PCR), and immunofluorescence staining. Neurobehavioral recovery was assessed through righting reflex, negative geotaxis, and Morris water maze tests. **Results:** M-R@siC-NPs exhibited a uniform size distribution (134 nm), good blood–brain barrier penetrability, and astrocyte-targeting specificity. The nanoparticles effectively silenced *circHIPK2* while demonstrating excellent colloidal stability and biosafety. *In vitro*, *circHIPK2* knockdown by M-R@siC-NPs markedly suppressed OGD-induced astrocyte activation, reducing GFAP and IL-1 β expression ($p < 0.01$). In HIBD mice, M-R@siC-NPs attenuated hippocampal astrocyte activation and improved motor coordination (shortened righting reflex latency, $p < 0.0001$) and spatial memory (increased platform crossings in Morris water maze, $p < 0.0001$). **Conclusions:** The RVG29/mannose dual-modified M-R@siC-NPs precisely regulated astrocyte activation and attenuated neuroinflammation, effectively ameliorating brain injury in HIBD mice. This study establishes a novel RNA interference-based therapeutic strategy for targeted neuroinflammatory modulation, providing a promising translational platform for HIE treatment.

Keywords: hypoxic–ischemic encephalopathy; lipid nanoparticles; astrocyte activation; *circHIPK2*; targeted gene therapy

1. Introduction

Neonatal hypoxic–ischemic encephalopathy (HIE), triggered by perinatal asphyxia, poses a critical threat to neonatal health and represents a major cause of neonatal mortality and childhood disability [1–4]. Its incidence ranges from 1–8% in developed countries and is reportedly as high as 26% in underdeveloped regions, with global mortality rates of 10–60%. Among survivors, at least 25% of affected infants suffer long-term neurodevelopmental sequelae, with 15–28% of pediatric cerebral palsy cases attributed to HIE [5,6]. The pathological mechanisms involve energy metabolism dysfunction, excitotoxicity, oxidative stress, neuroinflammation, and apoptosis.

Current therapeutic options for HIE remain limited. While therapeutic hypothermia—the clinical gold standard—has demonstrated neuroprotective effects via the

attenuation of astrocyte overactivation, 44–53% of treated infants still experience mortality or severe neurological deficits [7]. Stem cell transplantation, constrained by a narrow therapeutic window, dosage uncertainties, and individualized strategy challenges, faces limited clinical applicability [8]. These limitations underscore the urgent need for novel therapeutic approaches for HIE.

Astrocytes exhibit dual roles in central nervous system (CNS) inflammation [9–13]. While they are initially protective during lesion isolation and blood–brain barrier (BBB) restoration [14,15], they become harmful under ischemic stress in HIE. In the latter context, overactivated astrocytes release pro-inflammatory cytokines such as tumor necrosis factor- α (TNF- α) and interleukin-1 β (IL-1 β), disrupt BBB integrity, and amplify neuroinflammation, perpetuating a pathological cascade [16–20].



Circular RNAs (circRNAs), which are covalently closed structures lacking 5' caps and 3' poly(A) tails, have emerged as key regulators in brain disorders due to their exceptional stability [21–23]. For example, *circHIPK2* has been identified as a key regulator of astrocyte activation through a molecular mechanism involving miR-124-2HG sequestration and subsequent Sigma non-opioid intracellular receptor 1 (SIGMAR1)-mediated endoplasmic reticulum stress/autophagy pathway activation [24]. In lipopolysaccharide-induced neuroinflammation models, activation of the cortical *circHIPK2*/SIGMAR1 axis correlates with upregulated TNF- α and IL-1 β expression, whereas *circHIPK2* knockdown effectively suppresses astrocyte activation and inflammatory responses [25]. These findings suggest that *circHIPK2* silencing may represent a promising therapeutic strategy for HIE.

The BBB, although a critical protective mechanism, severely hinders drug delivery to the CNS [26–29]. RNA interference (RNAi) technology offers therapeutic potential, yet the application of small interfering RNA (siRNA) as a drug faces clinical translation challenges due to rapid *in vivo* degradation and poor cellular uptake [30,31]. Delivery of siRNA within nanocarriers can address these limitations through enhanced biocompatibility and modifiability, enabling efficient siRNA encapsulation and delivery [32,33]. Mesoporous silica nanoparticles (MSNs) offer tunable pore structures and high drug-loading capacity, making them promising gene vectors [34–38]. Lipid nanoparticles (LNPs) have been validated for safety and efficacy and shown to improve targeted delivery while minimizing off-target effects [32,39–41]. For example, glioma-targeting LNPs developed by Kuang *et al.* [42] demonstrated low systemic toxicity in clinical applications. However, delivery systems specifically for modulation of *circHIPK2* expression remain unexplored, hindering the translational progress for *circHIPK2*-based therapies.

Recent advances have highlighted RVG29, a 29-amino-acid peptide derived from rabies virus glycoprotein, as a BBB-penetrating ligand. 1,2-distearoyl-sn-glycero-3-phosphoethanolamine-poly (ethylene glycol)-neurotropic virus-derived peptide (DSPE-PEG2000-RVG29) binds to nicotinic acetylcholine receptors on endothelial cells of the BBB and facilitates receptor-mediated transcytosis [43–47]. Concurrently, overexpression of mannose receptor on astrocytes enables targeted delivery by mannose-decorated nanoparticles [48–51].

In the present study, we engineered a dual-targeted siRNA nanoplatfrom consisting of RVG29 peptide/mannose-functionalized LNPs loaded with *circHIPK2* siRNA (M-R@siC-NPs) as a potential therapy for HIE. This approach attempted to combine the advantages of LNPs and MSNs to achieve precise astrocyte targeting, suppress their pathological activation, and ameliorate neonatal hypoxic–ischemic brain injury. We tested the efficacy of M-R@siC-NPs both *in vitro* and *in vivo*,

and the results indicate that this innovative strategy may provide novel therapeutic avenues for HIE and advance RNAi-based targeted gene therapy.

2. Materials and Methods

2.1 Materials

Aminated dendritic MSNs (NH₂-MSNs, cat no. R-SG-89NH₂), 1,2-dipalmitoyl-sn-glycero-3-phosphocholine (DPPC, cat no. LP-R4-057), cholesterol, 1,2-distearoyl-sn-glycero-3-phosphoethanolamine-N-[methoxy(polyethylene glycol)-2000] (DSPE-PEG2000, cat no. R-H54510), DSPE-PEG2000-RVG29 (cat no. R9985), Cy5.5 (cat no. D10061), and M-PEG-lipid (cat no. LP-R4-18) were purchased from Ruixi Biotechnology Co., Ltd. (Xi'an, Shaanxi, China). Three siRNA (cat no. 15258) sequences targeting *circHIPK2* (*circHIPK2* siRNA) and a non-homologous negative control (siNC) without sequence homology to the target gene, along with fluorescein amidite (FAM)-labeled siRNA, were obtained from Qingke Biotechnology Co., Ltd. (Beijing, China). The siRNA-mate Plus transfection kit was acquired from GenePharma Co., Ltd. (cat no. G04026, Shanghai, China). Chloroform (CHCl₃, cat no. CX1060) and other analytical-grade reagents were sourced from Chongqing Chuandong Chemical Group Co., Ltd. (Chongqing, China). Fetal bovine serum (FBS) was acquired from Lanzhou Minhai Bio-Engineering Co.Ltd. (cat no. SA211.02, Lanzhou, Gansu, China). Dulbecco's Modified Eagle Medium/Nutrient Mixture F-12 (DMEM/F12, cat no. 11320033), and 0.25% trypsin-ethylenediaminetetraacetic acid (EDTA, cat no. 25200056) were purchased from Gibco BRL (Grand Island, NY, USA). The Cell Counting Kit-8 (CCK-8) was obtained from Boster Biological Technology Co., Ltd. (cat no. AR1199, Wuhan, Hubei, China). Trizol (cat no. RR036A), PrimeScript RT reagent Kit (cat no. RR092S), and SYBR Green PCR Master Mix (cat no. RR820A) were supplied by Takara Bio, Inc. (Shiga City, Shiga Prefecture, Japan). Quantitative real-time polymerase chain reaction (qPCR) primers (cat no. TSE20240906-029) were synthesized by ZerKcorp Biotech (Xi'an, Shaanxi, China). Agarose powder (cat no. GC205013), SerRed Nucleic Acid Stain (10,000 \times , water-soluble, cat no. G3606), phosphate-buffered saline (PBS, cat no. G4202), Tris-buffered saline with Tween 20 (TBST, cat no. G2157), Tris-glycine sodium dodecyl sulfate (SDS)-polyacrylamide gel electrophoresis (PAGE) high-resolution rapid electrophoresis (cat no. G2081)/transferring buffer (cat no. G2164), paraformaldehyde fixative (cat no. G1101), hematoxylin and eosin (H&E) staining solutions (cat no. G1076), and cell culture consumables were purchased from Servicebio (Wuhan, Hubei, China). C57BL/6 (C57) neonatal mice were obtained from the Lanzhou Veterinary Research Institute, Chinese Academy of Agricultural Sciences (Lanzhou, Gansu, China). Glial fibrillary acidic protein (GFAP) anti-

Table 1. siRNA sequences targeting circHIPK2.

Gene	Sense	Antisense
<i>sircHIPK2-1</i>	5'-GGAAGAGUAAGCAGCACCA-3'	5'-UGGUGCUGCUUACUCUCC-3'
<i>sircHIPK2-2</i>	5'-GAGACGGGAAUUAAGUCA-3'	5'-UUGACUUAUUCUCCGUCUC-3'
<i>sircHIPK2-3</i>	5'-GCUUAGUCUUUGAGAUGUU-3'	5'-AACAUCAAGACUAAGC-3'

siRNA, small interfering RNA; HIPK2, homeodomain-interacting protein kinase 2.

body (Abcam, cat no. ab7260, Shanghai, China; 1:10,000 dilution), IL-1 β antibody (Proteintech, Wuhan, Hubei, China; 1:5000 dilution), and glyceraldehyde-3-phosphate dehydrogenase (GAPDH) antibody (Proteintech, cat no. 60004-1-Ig, Wuhan, Hubei, China; 1:5000 dilution) were used for immunoblotting.

2.2 Screening of siRNAs Targeting circHIPK2

Specific siRNAs were designed to silence the expression of *circHIPK2*. The efficacy of *circHIPK2* silencing was evaluated using quantitative reverse transcription PCR (qRT-PCR) and western blotting. A total of four groups were established: three experimental groups transfected with each siRNA targeting *circHIPK2* (*circHIPK2-1*, *circHIPK2-2*, and *circHIPK2-3*) and one control group without siRNA transfection. The siRNA-mate Plus transfection reagent was used to deliver the siRNAs into astrocytes. The siRNA demonstrating the most efficient silencing effect was selected for subsequent experiments (Table 1).

2.3 Electrophoretic Mobility Shift Assay (EMSA)

Agarose gel electrophoresis was performed to evaluate the siRNA loading capacity of NH₂-MSNs. At room temperature, siRNA (218 μ g/mL) and NH₂-MSNs (5 mg/mL) were mixed at mass ratios (1:0, 1:10, 1:20, 1:25, 1:30, w/w), followed by incubation for 30 min. After incubation, 6 \times DNA loading buffer was added to the mixture. Samples were separated on a 3% agarose gel at 100 V for 20 min. The gel was visualized using a gel imaging system (version S2101237, ChampGel6000, Beijing, China) to observe band shifts of NH₂-MSN-siRNA complexes. The optimal binding ratio was determined to guide the preparation of M-R@siC-NPs.

2.4 Preparation of M-R@siC-NPs

Liposomes capable of crossing the BBB were prepared by mixing DPPC, cholesterol, M-PEG-lipid, and DSPE-PEG2000-RVG29 at a mass ratio of 3:1:1:1, dissolving the mixture in chloroform, and evaporating the solvent under vacuum to form a lipid film. The film was hydrated with 4 mL PBS and sonicated for 20 min to obtain a nanoemulsion. The emulsion was then emulsified under ice-cold conditions with 125 W ultrasonication for 8 min, followed by centrifugation at 6100 \times g for 10 min at 4 $^{\circ}$ C (repeated three times). The resulting product was purified via dialysis using a 100-nm cellulose membrane to obtain the liposomes.

For nanoparticle assembly, *circHIPK2* siRNA and NH₂-MSNs were mixed at a mass ratio of 1:30, incubated at room temperature for 10 min, and electrostatically bound to form NH₂-MSN-siRNA complexes. The liposomes were then combined with NH₂-MSN-siRNA at a 1:1 mass ratio, incubated at room temperature for 10 min, and subjected to ultrasonication (3 min pulses with 5-s intervals). After centrifugation at 6100 \times g for 10 min, the precipitate was resuspended and stored at 4 $^{\circ}$ C.

As controls, target-free LNPs (siC-NPs) were prepared using the same method but omitting DSPE-PEG2000-RVG29 and M-PEG-lipid. The full name of siC-NPs is non-targeted modified *circHIPK2* siRNA-lipid nanoparticles, which serve as non-targeted control nanoparticles in this study. Their core carrier components are consistent with those of M-R@siC-NPs (mannose/RVG29 peptide dual-modified *circHIPK2* siRNA-lipid nanoparticles), with the only difference being the lack of two targeted ligands, namely M-PEG-lipid and DSPE-PEG2000-RVG29. Both siC-NPs and M-R@siC-NPs carry *circHIPK2* siRNA3. Fluorescently labeled Cy5.5-conjugated targeting (Cy5.5-M-R@siC-NPs) and non-targeting nanoparticles (Cy5.5-siC-NPs) were also synthesized for fluorescence imaging.

2.5 Nanoparticle Characterization

The Malvern Nano analyzer (cat no. ZEN-3600, Zeta-Sizer, Malvern Instruments, Malvern, UK) was used to measure particle size and surface zeta potential. For sample preparation, 10 μ L of nanoparticle solution was spotted onto a 400-mesh carbon-coated copper grid, air-dried at room temperature, and imaged using transmission electron microscopy (TEM, cat no. HT7800, Hitachi, Tokyo Metropolis, Japan) to observe the morphology, structure, and size of NH₂-MSNs and M-R@siC-NPs.

2.6 Stability Assessment

The colloidal stability of M-R@siC-NPs was evaluated by monitoring hydrodynamic particle size changes via The Malvern Nano analyzer over 14 days (0, 2, 4, 6, 8, 10, 12, and 14 days). Additionally, M-R@siC-NPs suspensions were separately incubated in DMEM/F12 cell culture medium, PBS (pH 7.4), pure FBS, and artificial cerebrospinal fluid (aCSF) at ambient temperature (25 $^{\circ}$ C). Morphological changes, including macroscopic aggregation or precipitation, were observed and recorded daily for 14 days. This temperature represents the typical ambient temperature used for simulating the storage of nanoformu-

lations and *in vitro* experiments, and it is also consistent with the specifications on room temperature conditions for long-term stability testing as outlined in the “Guidelines for the Stability Testing of Pharmaceutical Preparations” of the Chinese Pharmacopoeia (25 °C ± 2 °C).

2.7 Encapsulation Efficiency and Drug Loading Capacity Determination

The siRNA concentration was quantified using a microvolume UV-Vis spectrophotometer (cat no. DENOVI DS-11, DENOVI, Wilmington, DE, USA) at 260 nm. Encapsulation efficiency (EE, %) was calculated via centrifugation (14,000 × g, 30 min) to separate unencapsulated siRNA. The formula used to calculate EE was:

$$EE(\%) = \frac{\text{Total siRNA in NPs} - \text{Free siRNA}}{\text{Total siRNA in NPs}} \times 100$$

Drug-loading capacity (DLC, %) was calculated using the following formula:

$$DLC(\%) = \frac{\text{Total siRNA in NPs} \times EE(\%)}{\text{Total lipid nanoparticle mass}} \times 100$$

2.8 Experimental Animals

C57BL/6 neonatal mice (specific pathogen-free grade) were purchased from Lanzhou Veterinary Research Institute, Chinese Academy of Agricultural Sciences. All histopathological evaluations were guided by faculty members specializing in pathology from the School of Basic Medical Sciences, Lanzhou University. The animal experimental protocols were approved by the Animal Ethics Committee of the Second Hospital of Lanzhou University (approval number: D2024-439).

2.9 Cell Viability Assay

Primary astrocytes were seeded into 96-well plates at a density of 1×10^4 cells/mL (100 µL per well). Edge wells were filled with sterile PBS to minimize edge effects. Cells were allowed to adhere for 24 h at 37 °C in an incubator with 5% CO₂. Solutions containing PBS (control), siC-NPs, and M-R@siC-NPs were prepared at gradient concentrations (0, 20, 40, 60, 80, 100, and 120 µg/mL). Primary astrocytes were treated with the respective solutions, with three replicates per group, and incubated for an additional 24 h. Prior to measurement, the supernatant was aspirated, and 10 µL of CCK-8 reagent was added to each well followed by 90 µL of serum-free medium. The plates were incubated in the dark for 2 h. Cell viability was assessed using a microplate reader (cat no. ELX808, Bio Tek Instruments, Inc., Windsor, VT, USA) across four groups (normal control (NC), oxygen-glucose deprivation (OGD), siC-NPs, M-R@siC-NPs) to evaluate nanoparticle cytotoxicity. During the culture and identification of astrocytes, detailed descriptions

have been provided regarding their cellular morphology and the expression of the specific marker GFAP, and the result of mycoplasma testing was confirmed to be negative.

2.10 Hemolysis Assay

Nanoparticle solutions (20, 40, 60, 80, and 100 µg/mL), PBS (negative control), or triple-distilled water (positive control) were added to 1.5-mL eppendorf tubes (1 mL per group). Blood was collected from the orbital venous plexus of healthy C57BL/6 mice using EDTA anticoagulant tubes. After mixing, the blood was centrifuged at 3000 × g for 15 min at room temperature. The plasma was discarded, and 20 µL of red blood cell pellet was resuspended in the respective solutions. The mixtures were incubated at 37 °C for 4 h before repeated centrifugation at 3000 × g for 15 min. The supernatant (100 µL) was transferred to a 96-well plate, and absorbance (optical density, OD) was measured at 540 nm using a microplate reader (Bio Tek Instruments, Inc.). Hemolysis rates were calculated using the standard formula:

$$\text{Hemolysis rate } (\%) = \frac{OD(\text{sample}) - OD(PBS)}{OD(ddH_2O) - OD(PBS)} \times 100\%$$

2.11 Toxicity Assessment

In strict accordance with the guidelines on non-clinical safety studies of pharmaceuticals issued by the International Council for Harmonisation of Technical Requirements for Pharmaceuticals for Human Use (ICH), these guidelines explicitly require that the potential effects of pharmaceuticals on major physiological functions (cardiovascular, respiratory, central nervous systems) be evaluated. Additionally, the study design and implementation refer to the Good Laboratory Practice for Non-Clinical Studies (GLP) promulgated by the National Medical Products Administration (NMPA) of China. Although this study does not belong to the anti-tumor field, the requirement in this guideline that nanopharmaceuticals should focus on carrier accumulation, organ-targeted distribution, and long-term toxicity is universally applicable. To evaluate the systemic toxicity of the nanoparticles, 10-day-old C57BL/6 neonatal mice were randomly divided into four groups (n = 3 per group, statistical analysis is conducted based on the complete set of sample data): a NC group, PBS group, siC-NPs group (80 µg/mL), and M-R@siC-NPs group (80 µg/mL). Nanoparticles were administered intravenously for 20 consecutive days. Blood samples were collected for complete blood count (CBC) analysis using a Mindray Veterinary Automated Hematology Analyzer (cat no. BC-2800vet, Mindray Biomedical Electronics Co., Ltd. Shenzhen, Guangdong, China). Serum was obtained via refrigerated centrifugation, and biochemical parameters were analyzed using an Automated Biochemical Analyzer (cat no. Chemray 240, Rayto Life Technology Co., Ltd. Shenzhen, Guang-

dong, China). Mice were anesthetized via intraperitoneal injection of 1% sodium pentobarbital at a dose of 50 mg/kg body weight. Anesthesia was confirmed when the mice exhibited no response to toe pinch and loss of corneal reflex. Subsequently, the mice were euthanized by cervical dislocation, in compliance with the Animal Ethics Guidelines of the Second Hospital of Lanzhou University. Death was verified by the absence of breathing and heartbeat for 5 consecutive minutes. After euthanasia, heart, liver, spleen, lung, kidney, and brain tissues were collected, fixed, and stained with H&E. Histopathological changes were quantitatively analyzed using the TissueFAXS Plus panoramic tissue cytometry system (cat no. TissueFAXS Plus, TissueGnostics GmbH, Vienna, Vienna State, Austria).

2.12 *In Vitro* Fluorescence Imaging

Primary astrocytes were seeded on confocal dishes at a density of 1×10^5 cells/mL and allowed to adhere overnight in an incubator. Experimental groups included: a PBS group, Cy5.5-siC-NPs group (80 μ g/mL), and Cy5.5-M-R@siC-NPs group (80 μ g/mL). After 24 h in culture, Hoechst 33258 (cat no. BL804A, Biosharp Biotechnology Co., Ltd. Nanjing, Jiangsu, China) was used to stain cell nuclei. Fluorescence imaging of the cells was performed 10 min after staining using a laser scanning confocal microscope (version ZEN Blue 2.3, Zeiss LSM880, Jena, Germany).

2.13 *In Vivo* Fluorescence Imaging

Ten-day-old C57BL/6 neonatal mice were randomly divided into three groups ($n = 9$ per group): a PBS group, Cy5.5-siC-NPs group, and Cy5.5-M-R@siC-NPs group. The corresponding agents were intraperitoneally injected into each group. At time points of 0, 1, 2, 4, 6, 8, 10, 12, 24, and 48 h post-injection, *in vivo* fluorescence imaging was performed using a small-animal imaging system (Vie-works Smart-LF, Eschborn, Hessen, Germany) to monitor nanoparticle accumulation and assess targeting specificity. Mice were euthanized when the peak intracranial fluorescence intensity was achieved, and brain tissues were harvested for *ex vivo* imaging. Heart, liver, spleen, kidney, and lung tissues were also collected and imaged using the Vie-works Smart-LF small-animal live imaging system to observe the Cy5 fluorescence distribution in major organs [52]. Brain tissue sections were further processed with 4',6-Diamidino-2-Phenylindole (DAPI, cat no. D1306, Thermo Fisher Scientific Inc. Waltham, MA, USA) staining for pathological examination.

2.14 Primary Astrocyte Isolation, Culture, and Characterization

Primary astrocytes were isolated from postnatal day 2–3 C57BL/6 neonatal mice anesthetized with isoflurane and disinfected with 75% ethanol. Whole brains were dissected under a biosafety cabinet, minced in pre-cooled

Hank's Buffered Salt Solution (HBSS) buffer, and digested with 0.25% trypsin-EDTA at 37 °C for 5 min. The digestion was halted by adding DMEM/F12 medium containing 10% FBS, followed by centrifugation at $1200 \times g$ for 5 min for the collection of cell pellets. Cells were resuspended and cultured at 37 °C in an incubator with 5% CO₂. After 3–4 days in culture, contaminating oligodendrocytes and microglia were removed by shaking at of the culture plates 260 rpm for 12 h using a THZ-98A thermomixer (cat no. THZ-98A, Shanghai Zhicheng Analytical Instrument Manufacturing Co., Ltd., Shanghai, China). High-purity astrocytes were characterized via GFAP immunofluorescence staining, according to the following procedure. Cells were fixed with 4% paraformaldehyde, permeabilized with 0.1% Triton X-100, incubated overnight with rabbit anti-GFAP primary antibody (1:10,000) at 4 °C, and labeled with Alexa Fluor 488-conjugated secondary antibody (1:1000, Invitrogen, Carlsbad, CA, USA) for 1 h at room temperature in the dark. Nuclei were counterstained with DAPI for 5 min. Stained samples were viewed using a Zeiss LSM880 laser scanning confocal microscope, and GFAP-positive cell proportions were quantified using ImageJ software (Version number: 1.54 g, NIH, Bethesda, MD, USA).

2.15 *In Vitro* and *In Vivo* Model Establishment

For the *in vitro* hypoxia-ischemia (HI) model, the cell culture medium was switched to serum-free medium 24 h before the cells were subjected to OGD. After two washes with PBS, the cells were incubated in serum-free and glucose-free medium and placed in a hypoxic chamber (1% O₂, 5% CO₂, 94% N₂, cat no. Coy-HC-05, Coy Laboratory Products, Inc. Grass Lake, MI, USA) at 37 °C for 6 h. The medium was then exchanged with complete medium for 24–48 h of recovery culture before collection for further analysis.

For the *in vivo* HIBD model, 6–8-day-old C57BL/6 neonatal mice were anesthetized with 2% isoflurane. The left common carotid artery was permanently ligated with an 8-0 surgical suture. Post-surgery, mice were exposed to a hypoxic environment (8% O₂, 92% N₂, flow rate 1.5 L/min) in a chamber for 2 h. Successful establishment of the HIBD model was verified using laser speckle imaging. Mice were randomized to four groups: the sham group, HIBD group, siC-NPs group, and M-R@siC-NPs group. Brain morphology was observed at 3, 5, and 7 days post-surgery. Brain tissues were collected, sectioned, and subjected to H&E staining and immunofluorescence analysis for assessment of pathological changes.

2.16 Western Blot Analysis

After treatment, brain tissues and cells were washed 2–3 times with pre-cooled PBS. Protein lysates were prepared using radioimmunoprecipitation assay (RIPA) lysis buffer (Ailv Life, AIWB-012, Wuhan, Hubei, China) containing protease inhibitors, incubated on ice for 30 min,

and centrifuged at $12,000 \times g$ for 20 min at 4°C for the collection of supernatant. Total protein concentration was determined using the BCA assay (PC0020, Solarbio, Beijing, China) and normalized. Equal amounts of proteins were separated by 10% SDS-PAGE and transferred to polyvinylidene difluoride (PVDF) membranes (Millipore, ISEQ00010, Darmstadt, Hessen, Germany). Membranes were blocked with QuickBlock blocking buffer (Servicebio, G2052-500ML) for 10 min at room temperature, followed by overnight incubation at 4°C with primary antibodies: GFAP (1:10,000), IL-1 β (Proteintech, 26048-1-AP; 1:5000), and GAPDH (Proteintech, CL594-60004; 1:5000). After washing with TBST, membranes were incubated with horseradish peroxidase (HRP)-conjugated secondary antibodies (1:5000) at room temperature for 1 h. Protein bands were detected using a chemiluminescence imaging system (cat no. Tanon 5200 Multi, Shanghai Tanon Science & Technology Co., Ltd., Shanghai, China), and gray value quantification analysis was performed using ImageJ software.

2.17 Behavioral Assessments

Mice in the siC-NPs and M-R@siC-NPs groups ($n = 12/\text{group}$) received intraperitoneal injections of LNPs (80 $\mu\text{g}/\text{mL}$) for 5 consecutive days, followed by a 2-day pause, totaling four cycles over 28 days (100 μL per dose). Post-treatment, three mice per group were euthanized for histopathological analysis, including H&E staining and GFAP immunofluorescence staining to assess glial activation. Samples from parallel groups ($n = 3/\text{group}$) were used for western blot analysis to quantify GFAP and IL-1 β expression in brain tissues.

2.17.1 Righting Reflex Test

This test was administered at the end of the first treatment cycle (day 5). Mice were placed ventral-side down on a soft pad, and the time to resume prone position was recorded (<60 s threshold). The results from three trials per mouse were averaged for analysis.

2.17.2 Negative Geotaxis Test

This test was conducted post-modeling at the end of the first treatment cycle (day 5). Mice were positioned head-down at a 15° incline on a 30-cm slope. Latency to complete a 180° turn toward the top was measured (cutoff: 60 s). The results from three trials per mouse were averaged.

2.17.3 Morris Water Maze

This test was performed on post-treatment day 28 using a 120-cm diameter pool (water depth: 50 cm, temperature: $21 \pm 1^\circ\text{C}$) containing a hidden platform (10-cm diameter, submerged 0.5 cm) in Quadrant 2. Six mice per group underwent four daily training sessions (120-s limit, 1-h intervals) over 4 days. On day 5, probe trials were initiated with platform removal. Target quadrant dwell time and swimming trajectories were tracked using the VisuTrack System (Shanghai Xinsoft, V3.0-2112, Shanghai, China).

2.18 Statistical Analysis

Statistical analysis was performed using GraphPad Prism 10.1.2 (GraphPad Software, Inc. La Jolla, CA, USA). All data are presented as mean \pm standard deviation (SD). Differences among multiple groups were compared using one-way analysis of variance (ANOVA) followed by Tukey's post-hoc test. Pairwise comparisons between two groups were performed using Student's *t*-test. Values of $p < 0.05$ indicated statistical significance.

3. Results

3.1 Screening of Silencing Sequences for *circHIPK2*

In the development of functional nanoparticles for this study, the first challenge was to identify highly efficient *circHIPK2* silencing sequences. For this purpose, primary astrocytes were transfected with three distinct *circHIPK2* siRNAs (*circHIPK2-1*, *circHIPK2-2*, and *circHIPK2-3*). FAM-labeled siRNAs were utilized to track transfection efficiency (Fig. 1A). qRT-PCR results showed that compared with the Control group (without siRNA transfection), all three *circHIPK2* siRNAs significantly reduced the expression level of *circHIPK2* mRNA in primary astrocytes. Among them, *circHIPK2 siRNA-3* exhibited the optimal silencing efficiency, mediating an 80.13% decrease in *circHIPK2* mRNA expression. This efficiency was significantly higher than that of *circHIPK2 siRNA-1* and *circHIPK2 siRNA-2*, with a statistically significant difference ($p < 0.0001$), confirming that siRNA3 has the strongest ability to specifically recognize and degrade the target gene mRNA (Fig. 1D). We further evaluated the effect of the three siRNAs on GFAP expression via Western blot. The results demonstrated that the GFAP protein expression in the *circHIPK2 siRNA-3* group was 40% lower than that in the Control group. This inhibitory effect was significantly more pronounced than those in the *siRNA-1* and *siRNA-2* groups ($p < 0.001$), and was positively correlated with the high degradation efficiency at the mRNA level (Fig. 1B,C). These findings confirm that the silencing effect of *siRNA-3* can be effectively transmitted to the protein expression level, forming a complete functional chain of gene silencing functional inhibition. *circHIPK2 siRNA-3* is identified as the optimal sequence for silencing *circHIPK2*, with its gene sequences being 5'-GCUUAGUCUUUGAGAUGUU-3' (sense strand) and 5'-AACAUCUCAAAGACUAAGC-3' (antisense strand). Based on these findings, *circHIPK2-3* was selected for use in the subsequent experiments.

3.2 Characterization of Nanoparticles

The physicochemical properties of the different synthesized nanoparticles are summarized in Fig. 2. Dynamic

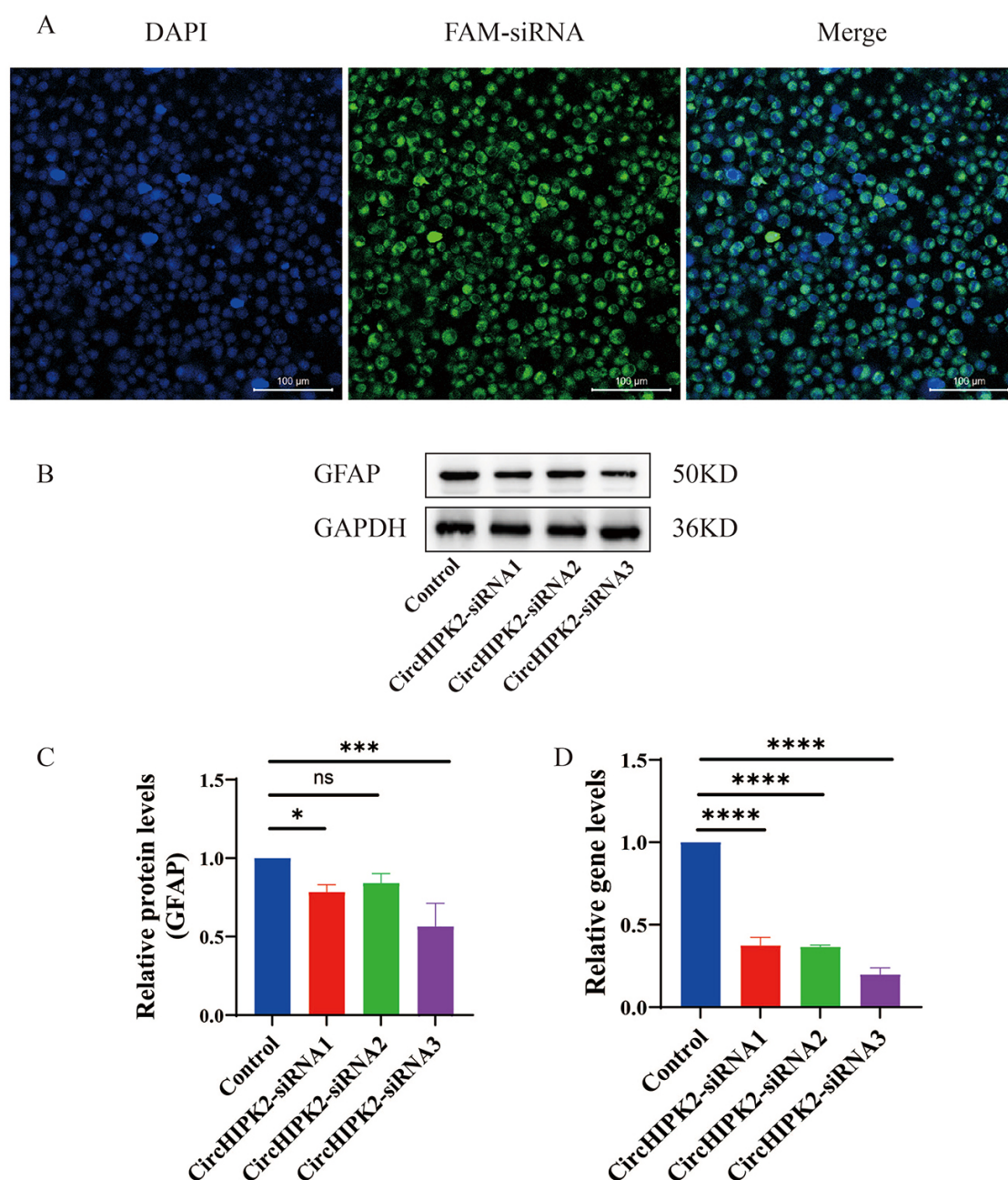


Fig. 1. Silencing efficiency of three different *circHIPK2* siRNA sequences in astrocytes. (A) Cellular localization of FAM-labeled siRNAs (green fluorescence) at 48 h post-transfection, with nuclei counterstained by DAPI (blue). Scale bar = 100 μ m. (B) Western blot analysis of glial fibrillary acidic protein (GFAP) protein expression across groups. GAPDH served as a loading control. (C) Quantitative analysis of GFAP protein levels normalized to GAPDH expression ($n = 3$). (D) Quantitative reverse transcription PCR (qRT-PCR) analysis of *circHIPK2* mRNA expression ($n = 3$). Data are presented as mean \pm SD. Statistical significance was determined by one-way ANOVA with Tukey's post-hoc test (ns $p \geq 0.05$; * $p < 0.05$; *** $p < 0.001$; **** $p < 0.0001$ vs. control group). FAM, fluorescein amidite.

light scattering (DLS) analysis revealed that the hydrodynamic diameters of the NH₂-MSNs, NH₂-MSN-siRNA, and M-R@siC-NPs were 115.80 ± 9.65 nm, 118.40 ± 7.21 nm, and 134.78 ± 10.25 nm, respectively, with polydispersity index (PDI) values of 0.206 ± 0.041 , 0.211 ± 0.019 , and 0.205 ± 0.089 , respectively (Fig. 2A). The narrow PDI

values indicated homogeneous particle size distribution and high-quality synthesis. Zeta potential measurements further demonstrated surface charges of 20.00 ± 0.24 mV for NH₂-MSNs, -3.2 ± 0.86 mV for NH₂-MSN-siRNA, and 4.3 ± 0.48 mV for M-R@siC-NPs (Fig. 2B). The transition from positive to negative zeta potentials confirmed electrostatic

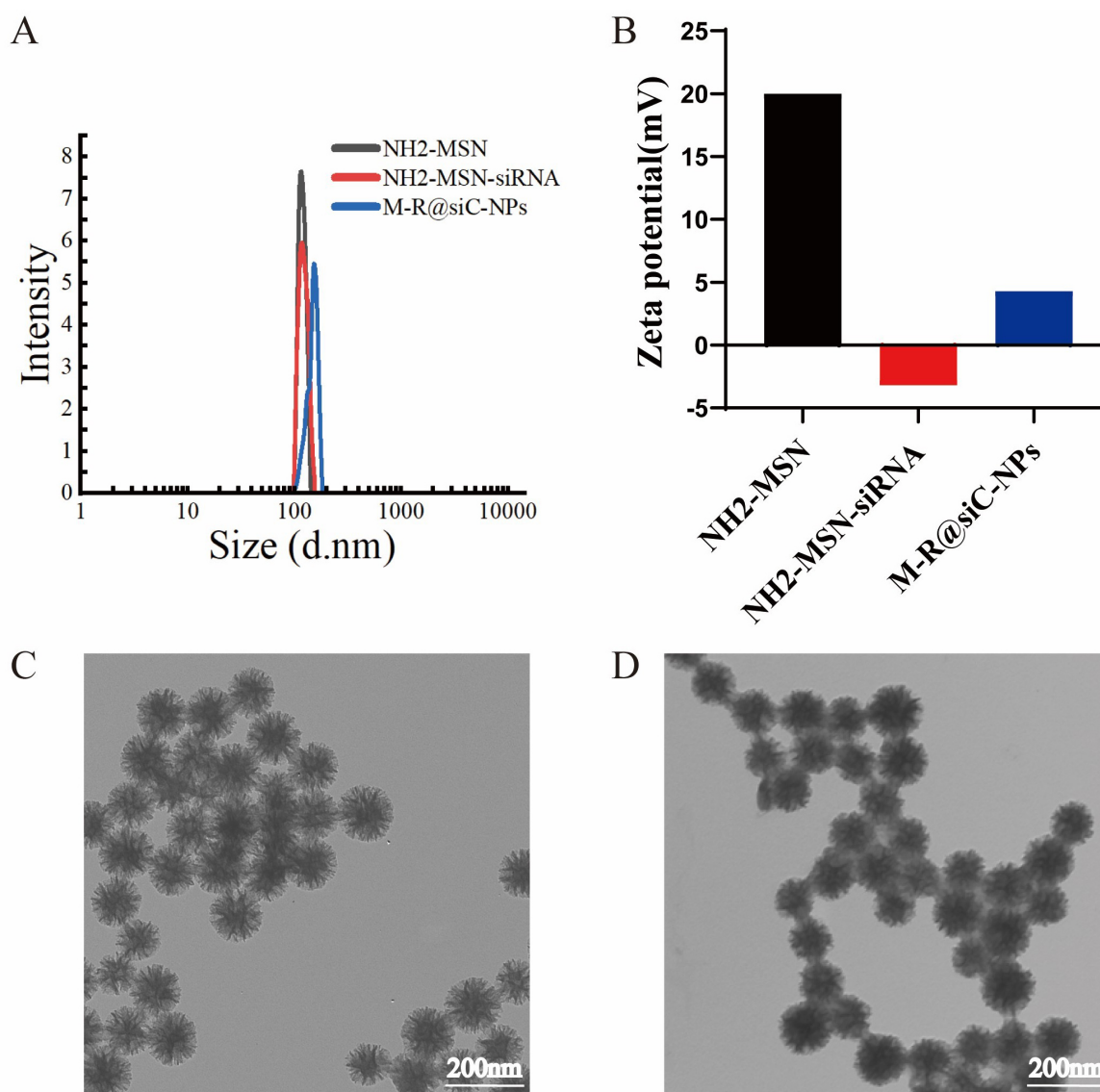


Fig. 2. Physicochemical characterization of nanoparticles. (A) Hydrodynamic size distribution of different nanoparticle formulations ($n = 3$; data presented as mean \pm SD). (B) Zeta potential analysis of nanoparticles (25 °C, dispersed in deionized water, $n = 3$). (C,D) TEM images of NH₂-MSNs (C) and M-R@siC-NPs (D), showcasing morphological features and dispersion homogeneity. Scale bar = 200 nm. TEM, transmission electron microscopy; NH₂-MSNs, aminated dendritic MSNs; M-R@siC-NPs, mannose-RVG29@CircHIPK2siRNA-NPs.

binding between the positively charged NH₂-MSNs and negatively charged siRNA. TEM images revealed spherical morphologies for both NH₂-MSNs (Fig. 2C) and M-R@siC-NPs (Fig. 2D), with uniform diameters less than 200 nm and no apparent aggregation or fragmentation. The consistent particle size, comparable zeta potentials, and excellent colloidal stability of M-R@siC-NPs align with the requirements for biomedical applications. These physicochemical properties are critical for the performance of these nanoparticles in subsequent gene delivery and biosensing experiments, influencing parameters such as blood circulation time, cellular uptake, and biodistribution.

3.3 Encapsulation Efficiency and Drug Loading Capacity of Nanoparticles

To determine the optimal mass ratio for binding *circHIPK2* siRNA (218 μ g/mL) with NH₂-MSNs (5 mg/mL), agarose gel electrophoresis was performed. The results demonstrated that when the mass ratio of siRNA to NH₂-MSNs reached 1:30 or higher, the fluorescence intensity of the siRNA band decreased (Fig. 3A), indicating successful electrostatic binding between the positively charged NH₂-MSN and negatively charged siRNA. Thus, a 1:30 mass ratio was employed in the preparation of nanoparticles for subsequent experiments. To evaluate the encapsulation efficiency and drug loading capacity of the nanoparti-

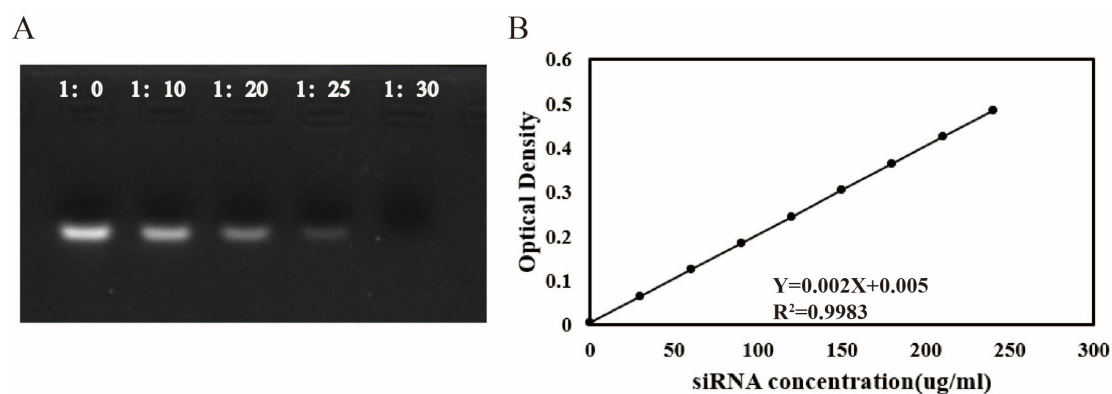


Fig. 3. Characterization of siRNA encapsulation efficiency and drug loading capacity of nanoparticles. (A) Agarose gel electrophoresis analysis of *circHIPK2* siRNA binding to amino-functionalized dendritic silica nanoparticles (NH₂-MSNs) at varying mass ratios (1:0, 1:10, 1:20, 1:25, and 1:30). Disappearance of the siRNA band intensity indicates successful loading. (B) Standard curve for siRNA quantification: absorbance at 260 nm was measured for gradient siRNA solutions, yielding a linear regression equation of $Y = 0.002X + 0.005$ ($R^2 = 0.9983$, $n = 3$; data presented as mean \pm SD).

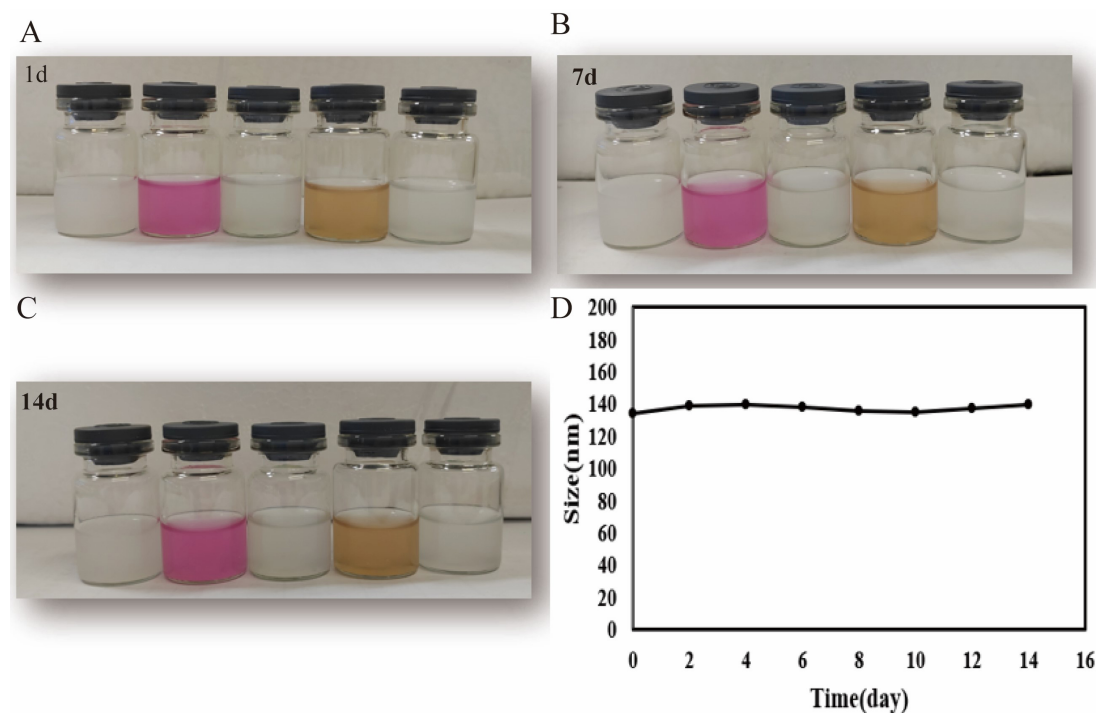


Fig. 4. Physical stability of M-R@siC-NPs in various media. (A–C) Macroscopic appearance of undiluted original dispersions of M-R@siC-NPs stored in DMEM/F12 medium, PBS, FBS, and aCSF on days 1, 7, and 14 (stored at 25 °C in the dark). No visible aggregation or precipitation was observed in any medium, confirming the excellent colloidal stability of the M-R@siC-NPs. (D) Hydrodynamic size evolution of M-R@siC-NPs measured by DLS over 14 days ($n = 3$; data presented as mean \pm SD). PBS, phosphate-buffered saline; FBS, fetal bovine serum; aCSF, artificial cerebrospinal fluid; DLS, dynamic light scattering.

cles, ultramicroscopic UV-Vis spectrophotometry was used to quantify siRNA content ($R^2 = 0.9983$). The calculated encapsulation efficiency and drug loading capacity were $75.28\% \pm 0.06\%$ and $15.63\% \pm 0.27\%$, respectively (Fig. 3B).

3.4 Stability of Nanoparticles

To evaluate the stability and biocompatibility of nanoparticles in physiological environments, the morphology and dispersion of nanoparticle suspensions in DMEM/F12, PBS, FBS, and aCSF were observed over 14 days. The results demonstrated that M-R@siC-NPs maintained a uniform dispersion without significant aggre-

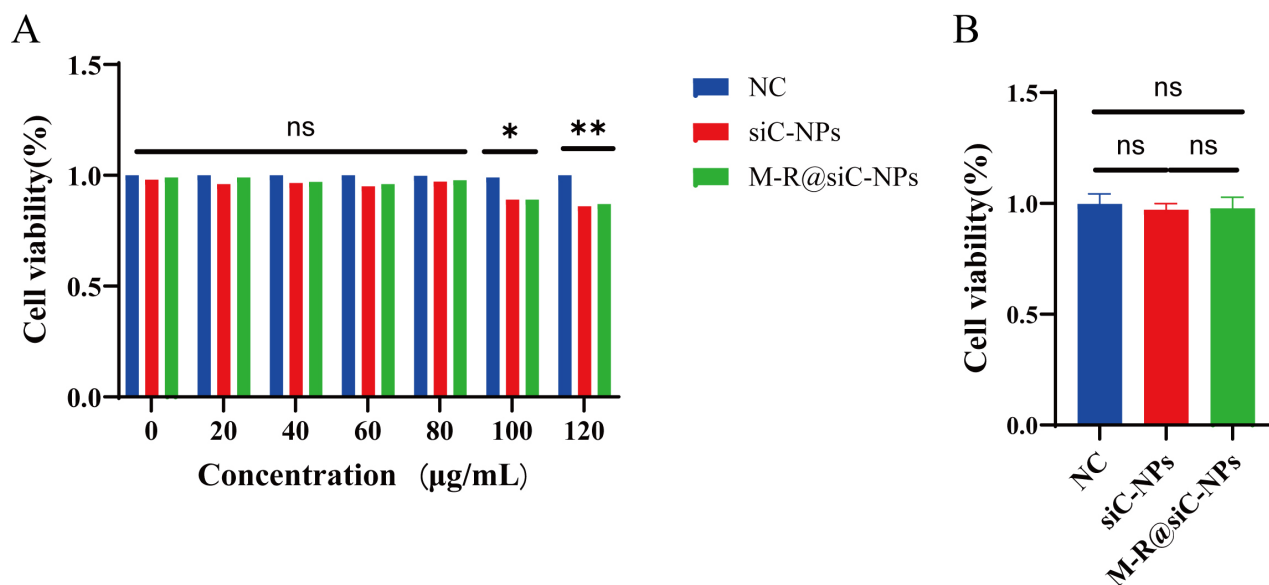


Fig. 5. Nanoparticle cytotoxicity assessment for astrocytes. (A) Effects of different concentrations (20, 40, 60, 80, 100, and 120 μg/mL) of NC (normal control) group, siC-NPs, and M-R@siC-NPs on astrocyte viability, assessed by CCK-8 assay ($n = 3$; data presented as mean \pm SD). (B) No significant cytotoxicity was observed for siC-NPs and M-R@siC-NPs at 80 μg/mL compared with the NC group. Statistical significance was determined by one-way ANOVA with Tukey's post-hoc test (ns: $p \geq 0.05$; * $p < 0.05$; ** $p < 0.01$). CCK-8, Cell Counting Kit-8.

gation or precipitation in all tested media. Notably, no evident interaction between nanoparticles and serum proteins or culture medium components was observed in FBS and DMEM/F12, confirming effective surface modification (Fig. 4A–C). These findings indicate that M-R@siC-NPs exhibit excellent long-term stability, making them suitable for *in vitro* cell culture and *in vivo* CNS delivery applications. Additionally, DLS analysis revealed no significant fluctuations in the hydrodynamic diameter of M-R@siC-NPs throughout the 14-day study period ($p \geq 0.05$, Fig. 4D). Particle size measurements at specific time points (day 0, 2, 4, 6, 8, 10, 12, and 14) were as follows: 134.78 ± 10.25 nm, 135.12 ± 9.87 nm, 136.54 ± 10.13 nm, 137.21 ± 9.92 nm, 136.89 ± 10.31 nm, 137.56 ± 10.05 nm, 138.12 ± 9.78 nm, and 138.45 ± 10.22 nm. These consistent measurements further confirm the structural integrity of M-R@siC-NPs under physiological conditions.

3.5 Nanoparticle Biocompatibility

3.5.1 *In Vitro* Biocompatibility Assessment

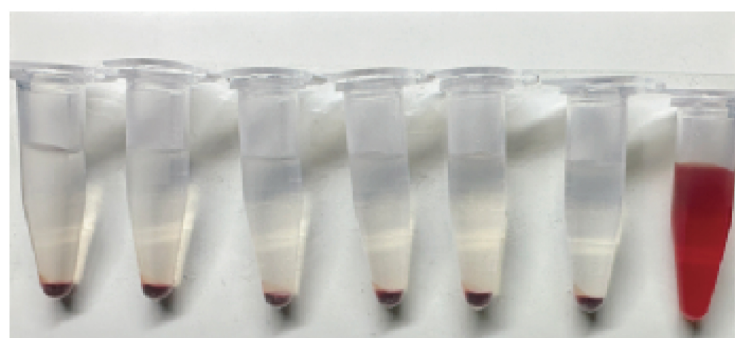
The biocompatibility of LNPs was evaluated by adding them to cultures of primary astrocytes for 24 h, followed by cell viability analysis using the CCK-8 assay. The results demonstrated that astrocytes retained over 90% cell viability upon exposure to siC-NPs and M-R@siC-NPs at concentrations of 20–80 μg/mL. However, with nanoparticle concentrations of 100 μg/mL, astrocyte viability decreased to 89.01% (siC-NPs) and 87.59% (M-R@siC-NPs), and these reductions were significant compared with the vi-

ability of the control group (Fig. 5A). Based on these findings, 80 μg/mL was selected as the optimal concentration for subsequent experiments to ensure the biocompatibility of nanoparticle treatments (Fig. 5B).

3.5.2 *In Vivo* Biocompatibility Assessment

To evaluate the *in vivo* safety of the nanoparticles, a peripheral blood hemolysis assay was conducted to assess whether free nanoparticles in the bloodstream would induce acute erythrocyte destruction. At nanoparticle concentrations of 20, 40, 60, 80, and 100 μg/mL, the hemolysis rates remained less than 1.5% (Fig. 6A,B). From the appearance of centrifuged samples in Fig. 6A, the supernatants of all nanoparticle concentration groups remained colorless and transparent, which was completely consistent with the PBS negative control group. In contrast, the dark red supernatant observed in the positive control group (triple-distilled water) was absent in all nanoparticle groups. This macroscopic result directly confirms that even at the highest tested concentration (100 μg/mL), the nanoparticles did not induce visible red blood cell (RBC) lysis, indicating no significant hemolysis and initially verifying their hemocompatibility (Fig. 6A). The absorbance of the supernatants was measured at a wavelength of 540 nm using a microplate reader, and the hemolysis rate was calculated according to the formula. The results showed that the hemolysis rate of each concentration group was below 1.5%, which was far lower than the 5% safety threshold for hemolysis rate of biomaterials (Fig. 6B). The slight

A



PBS 20µg/mL 40µg/mL 60µg/mL 80µg/mL 100µg/mL H2O

B

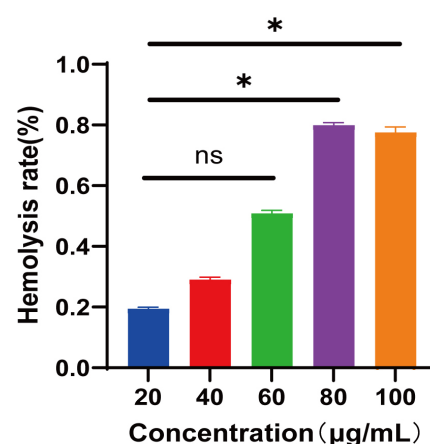


Fig. 6. Hemolysis assessment upon nanoparticle exposure. (A) Hemolysis assay setup: (left to right) negative control (1 mL PBS), nanoparticle-treated groups (20, 40, 60, 80, or 100 µg/mL), and positive control (1 mL ddH₂O). After incubation at 37 °C for 3 h, samples were centrifuged to observe hemolysis (red supernatant indicates erythrocyte lysis). (B) Concentration-dependent hemolysis rates (n = 3; data presented as mean ± SD). Statistical significance was determined by one-way ANOVA with Dunnett's post-hoc test (ns: $p \geq 0.05$; * $p < 0.05$ vs. PBS group).

upward trend of hemolysis rate with increasing concentration was attributed to the slightly increased probability of non-specific contact between nanoparticles and RBC membranes as the nanoparticle concentration increased (from 20 to 100 µg/mL). This contact led to the release of a minimal amount of hemoglobin; however, the release volume was extremely low and did not reach the threshold for macroscopically visible color changes. These results confirmed that the nanoparticles did not induce erythrocyte destruction, indicating they offer an excellent *in vivo* safety profile.

For *in vivo* analysis of nanoparticle biocompatibility, this study evaluated the functional status of major physiological organs in experimental animals after daily intravenous injection of nanoparticles for 20 days. Blood routine parameters (white blood cell [WBC] count, red blood cell [RBC] count, hemoglobin [HGB], and platelet [PLT] count) and serum biochemical markers (alanine aminotransferase [ALT], aspartate aminotransferase [AST], total bilirubin [TBIL], albumin [ALB], alkaline phosphatase [ALP], creatinine [CREA], blood urea nitrogen [BUN], and uric acid [UA]) were analyzed in both control and LNP-treated groups. All values fell within the reference ranges for healthy mice, with no adverse effects observed (Fig. 7). Statistical analysis revealed no significant differences between groups ($p > 0.05$), collectively indicating that the LNP complexes exhibited no detectable hepatotoxicity or nephrotoxicity.

To assess the *in vivo* biosafety of the LNPs, histopathological analysis was performed on major organs (heart, liver, spleen, lung, kidney, and brain) harvested after

20 days of intravenous injection of the different particles. The H&E staining results demonstrated that, compared with the NC group, the nanoparticle-treated groups exhibited no significant histopathological abnormalities, showing no inflammatory cell infiltration, cellular edema, or necrosis in any organ (Fig. 8). These morphological observations confirmed that the LNPs caused no detectable cytotoxicity or structural damage to vital organs, underscoring their excellent *in vivo* biocompatibility and safety profile.

3.6 Nanoparticle Targeting Efficiency

3.6.1 *In Vitro* Targeting Assessment

Evaluations of cellular nanoparticle uptake efficiency and targeting revealed distinct fluorescence patterns. No fluorescent signals were detected in the PBS control group under laser scanning confocal microscopy (LSCM). In contrast, significant intracellular fluorescence accumulation was observed in the groups treated with Cy5.5-siC-NPs (80 µg/mL) and Cy5.5-M-R@siC-NPs (80 µg/mL). Quantitative analysis demonstrated that the mean fluorescence intensity in these experimental groups was statistically higher than that in the control group (Fig. 9A,B), with cellular uptake efficiency reaching $95.2\% \pm 2.7\%$. These results confirm that the LNP carriers effectively penetrate cell membranes and thus, offer sufficient transmembrane transport capacity.

On the evaluation of the targeted delivery performance of the nanoparticles, the surface-modified Cy5.5-M-R@siC-NPs exhibited distinct advantages. LSCM imaging revealed significantly stronger fluorescence signals in the

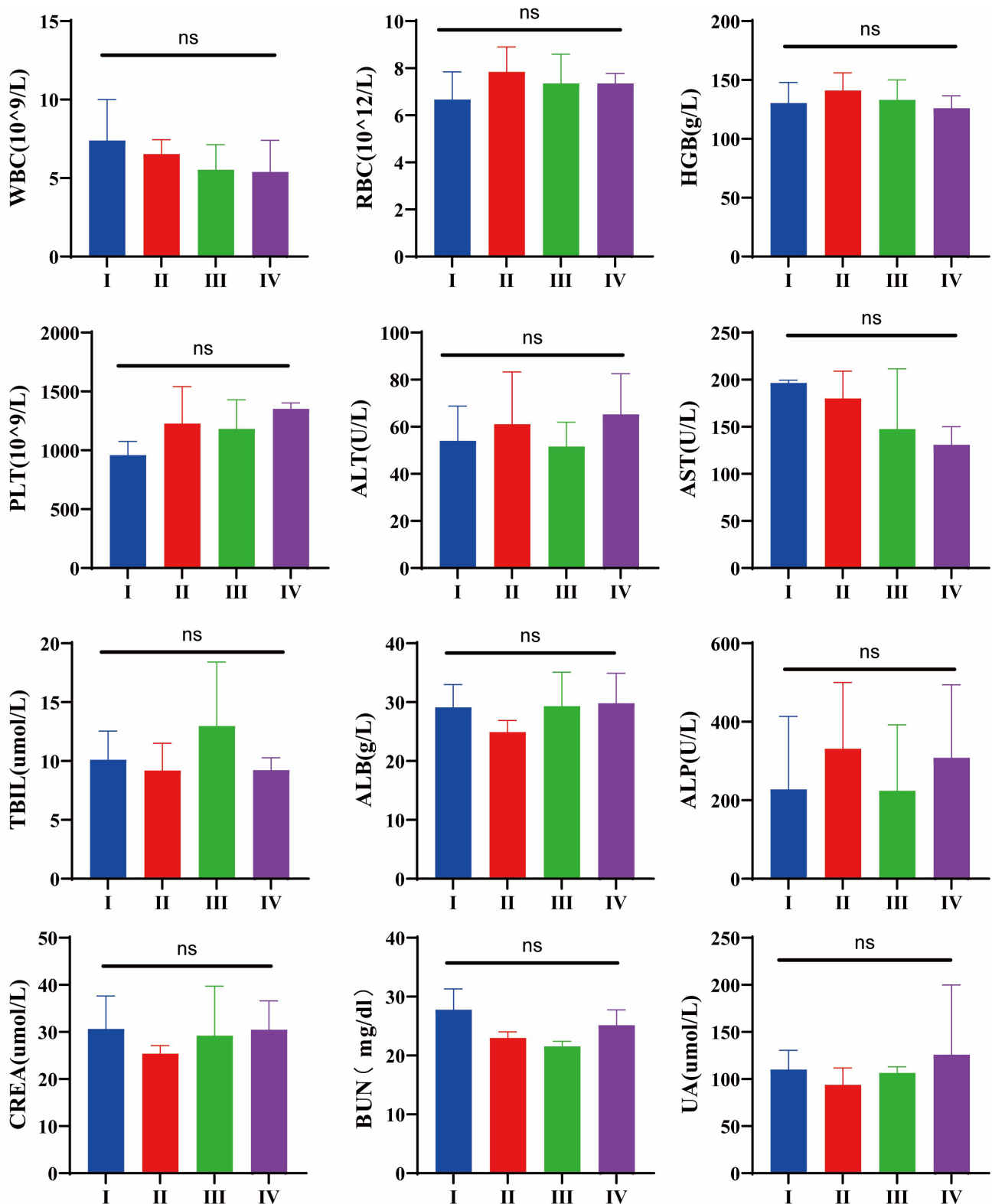


Fig. 7. Toxicological evaluation of routine blood parameters and hepatic/renal function indicators after exposure to different conditions. (I) NC (normal control) group, (II) PBS-treated group, (III) siC-NPs-treated group, (IV) and M-R@siC-NPs-treated group. No significant differences were observed in routine blood parameters (WBC count, RBC count, HGB, and PLT count) or hepatic/renal biochemical markers (ALT, AST, TBIL, ALB, ALP, CREA, BUN, and UA) across the groups (ns: $p \geq 0.05$). WBC, white blood cell; RBC, red blood cell; HGB, hemoglobin; PLT, platelet; ALT, alanine aminotransferase; AST, aspartate aminotransferase; TBIL, total bilirubin; ALB, albumin; ALP, alkaline phosphatase; CREA, creatinine; BUN, blood urea nitrogen; UA, uric acid.

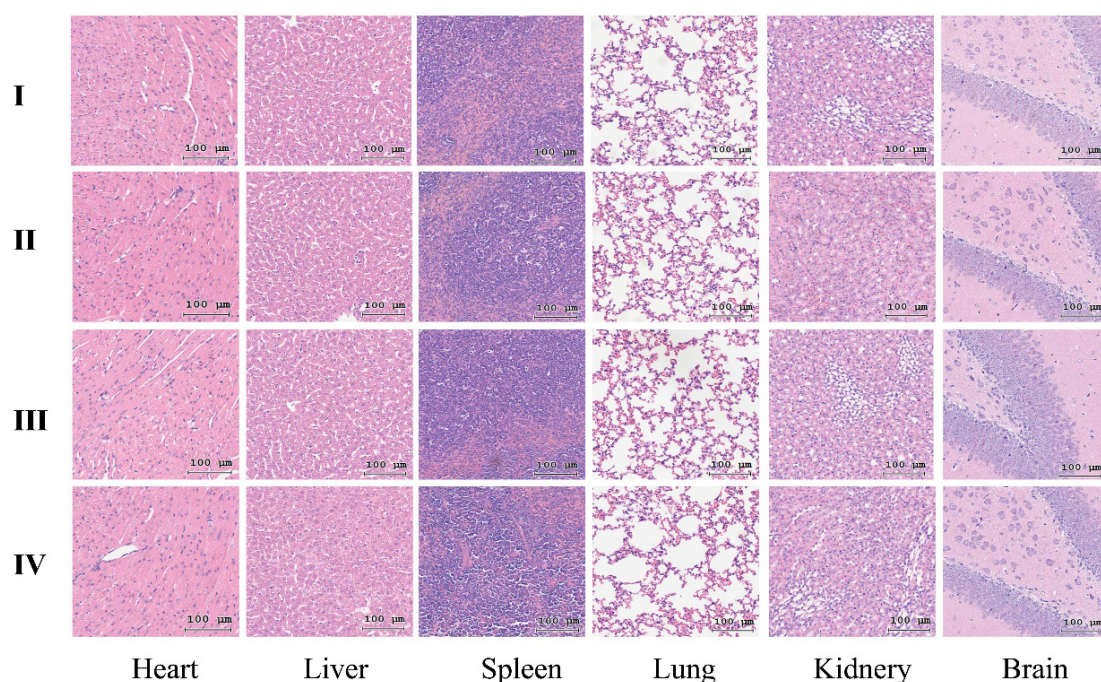


Fig. 8. Histopathological analysis of major organs via H&E staining after exposure to nanoparticles in different experimental groups. (I) NC group, (II) PBS-treated group, (III) siC-NPs-treated group, and (IV) M-R@siC-NPs-treated group. Scale bars = 100 μ m. H&E, hematoxylin and eosin.

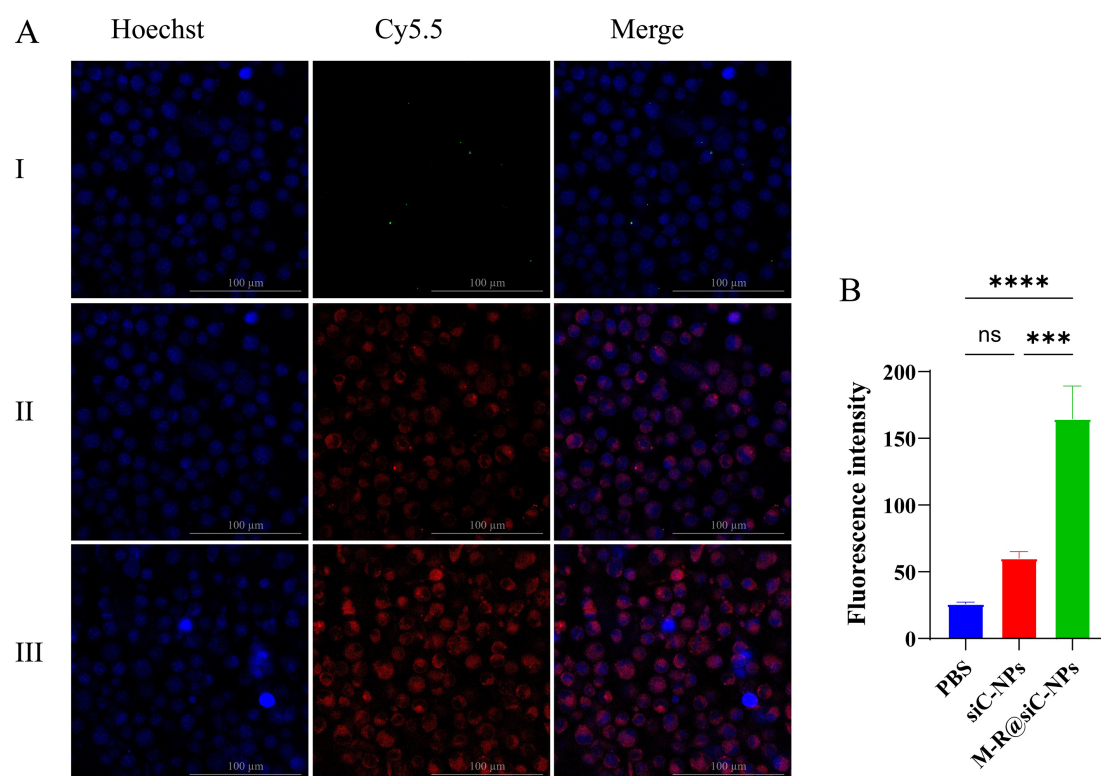


Fig. 9. *In vitro* targeting evaluation. (A) LSCM images showing the localization of Cy5.5-labeled siC-NPs (Group II) and Cy5.5-M-R@siC-NPs (Group III) in astrocytes. Red fluorescence (Cy5.5) indicates nanoparticle distribution, while blue fluorescence (DAPI) labels cell nuclei. Scale bar = 100 μ m. (B) Quantitative analysis of fluorescence intensity in Groups I (PBS control), II (Cy5.5-siC-NPs), and III (Cy5.5-M-R@siC-NPs). Data are presented as mean \pm SD ($n = 3$). Statistical significance was determined by one-way ANOVA with Tukey's post-hoc test (ns $p \geq 0.05$; *** $p < 0.001$; **** $p < 0.0001$ vs. control group). LSCM, laser scanning confocal microscopy.

group treated with Cy5.5-M-R@siC-NPs compared with that treated with Cy5.5-siC-NPs. Fluorescence quantification confirmed that the intensity of Cy5.5-M-R@siC-NPs was three-fold higher than that of Cy5.5-siC-NPs (Fig. 9A,B), with a statistically significant difference observed. This outcome substantiates that the active targeting capability of M-R@siC-NPs can achieve drug delivery specificity.

3.6.2 *In Vivo* Targeting Efficiency Evaluation

In vivo live imaging revealed that intraperitoneally administered targeted nanoparticles (Cy5.5-M-R@siC-NPs) exhibited peak fluorescence intensity in the brain at 4 hours post-injection, with complete clearance observed by 48 hours (Fig. 10A-III). In contrast, non-targeted Cy5.5-siC-NPs displayed a delayed peak fluorescence at 6 hours, reduced intensity, and rapid clearance within 24 hours (Fig. 10A-II,C). Statistical analysis demonstrated that the brain accumulation of targeted nanoparticles was significantly higher than that of the non-targeted counterparts from 4–10 hours post-administration. These results confirm that the M-R@siC-NPs with brain-targeting modifications effectively penetrated the BBB, potentially offering enhanced cerebral bioavailability and an extended therapeutic window.

Ex vivo fluorescence quantification further validated the brain-specific targeting efficacy of the modified nanoparticles (Fig. 10). Quantitative analysis of brain tissues revealed markedly stronger Cy5.5-M-R@siC-NPs fluorescence compared with Cy5.5-siC-NPs fluorescence (Fig. 10B,D), underscoring their superior BBB-penetrating capacity. Systemic biodistribution analysis (Fig. 10B,E) showed uniform distribution of the non-targeted nanoparticles across major organs, whereas Cy5.5-M-R@siC-NPs demonstrated selective enrichment in the brain, with statistically significant differences in fluorescence intensity observed. The results of this spatial distribution analysis support the notion that the brain-targeting ligands on M-R@siC-NPs minimize peripheral organ exposure while enhancing brain-specific delivery.

Microscopic localization in brain tissues provided insight into the BBB-penetration mechanism of M-R@siC-NPs (Fig. 11). Frozen sections stained with DAPI (blue fluorescence, nuclear counterstain) revealed distinct red fluorescence signals from Cy5.5-M-R@siC-NPs, with pronounced accumulation in the brain parenchyma and perivascular regions. Compared with controls and non-targeted nanoparticles, targeted nanoparticles exhibited concentrated fluorescence in the brain parenchyma, particularly near the BBB. The BBB restricts passive diffusion of most molecules; however, the enhanced retention of Cy5.5-M-R@siC-NPs in brain tissues suggests active transport mechanisms. The unique lipid composition and surface modifications of these nanoparticles likely enable receptor-mediated interactions with endothelial cells lining

the BBB, facilitating transcytosis and sustained cerebral retention (Fig. 11).

3.7 Cellular Experiments to Test the Therapeutic Efficacy of M-R@siC-NPs

3.7.1 Characterization of Primary Astrocytes

Primary astrocytes were successfully isolated and purified from the cerebral tissues of C57BL/6 neonatal mice. Immunofluorescence staining confirmed astrocyte identity: GFAP-labeled astrocytic processes (green, Fig. 12A-I), phalloidin-stained F-actin cytoskeleton (red, Fig. 12A-II), and DAPI-stained nuclei (blue, Fig. 12A-III). Merged images (Fig. 12A-IV) revealed that primary astrocytes exhibited characteristic star-shaped or polygonal morphology with large cell bodies, prominent nuclei, and multiple filopodia-like processes in culture. Quantitative analysis demonstrated that >90% of cells displayed strong GFAP positivity in both the cell body and processes. Statistical results confirmed a purity of 94.65% GFAP-positive cells (Fig. 12B,C), confirming high-quality astrocyte cultures.

3.7.2 *In Vitro* Therapeutic Efficacy Evaluation

To assess the therapeutic potential of M-R@siC-NPs, primary astrocytes were subjected to OGD treatment. The experimental groups included NC, OGD (model), siC-NPs-treated, and M-R@siC-NPs-treated groups. The outcomes were evaluated based on GFAP expression, IL-1 β level, and cell viability via CCK-8 assay (Fig. 13A–D).

In the OGD model of primary astrocytes, Western blot results demonstrated that the OGD model group exhibited significantly increased protein levels of GFAP and IL-1 β . This elevation was attributed to astrocyte activation and subsequent inflammation triggered by hypoxia-ischemia, confirming the successful establishment of the OGD model. After treatment with siC-NPs and M-R@siC-NPs, siC-NPs slightly reduced the expression of GFAP and IL-1 β , while M-R@siC-NPs showed a significantly superior inhibitory effect (Fig. 13A–C, the original western blot images can be found in the **Supplementary Materials**). This difference stemmed from the dual modification of M-R@siC-NPs with M-PEG-lipid and DSPE-PEG2000-RVG29. Specifically, this dual modification enhanced the targeting ability of M-R@siC-NPs to astrocytes and improved their cellular uptake efficiency, thus confirming that targeted modification is the core factor for enhancing *in vitro* therapeutic efficacy. The CCK-8 assay results further showed that OGD exposure drastically reduced cell viability, whereas treatment with siC-NPs partially restored viability. Notably, M-R@siC-NPs treatment resulted in the most significant recovery of cell viability (Fig. 13D).

These findings demonstrate that M-R@siC-NPs can alleviate astrocyte activation and neuroinflammation via targeted gene silencing, while promoting the functional recovery of damaged cells.

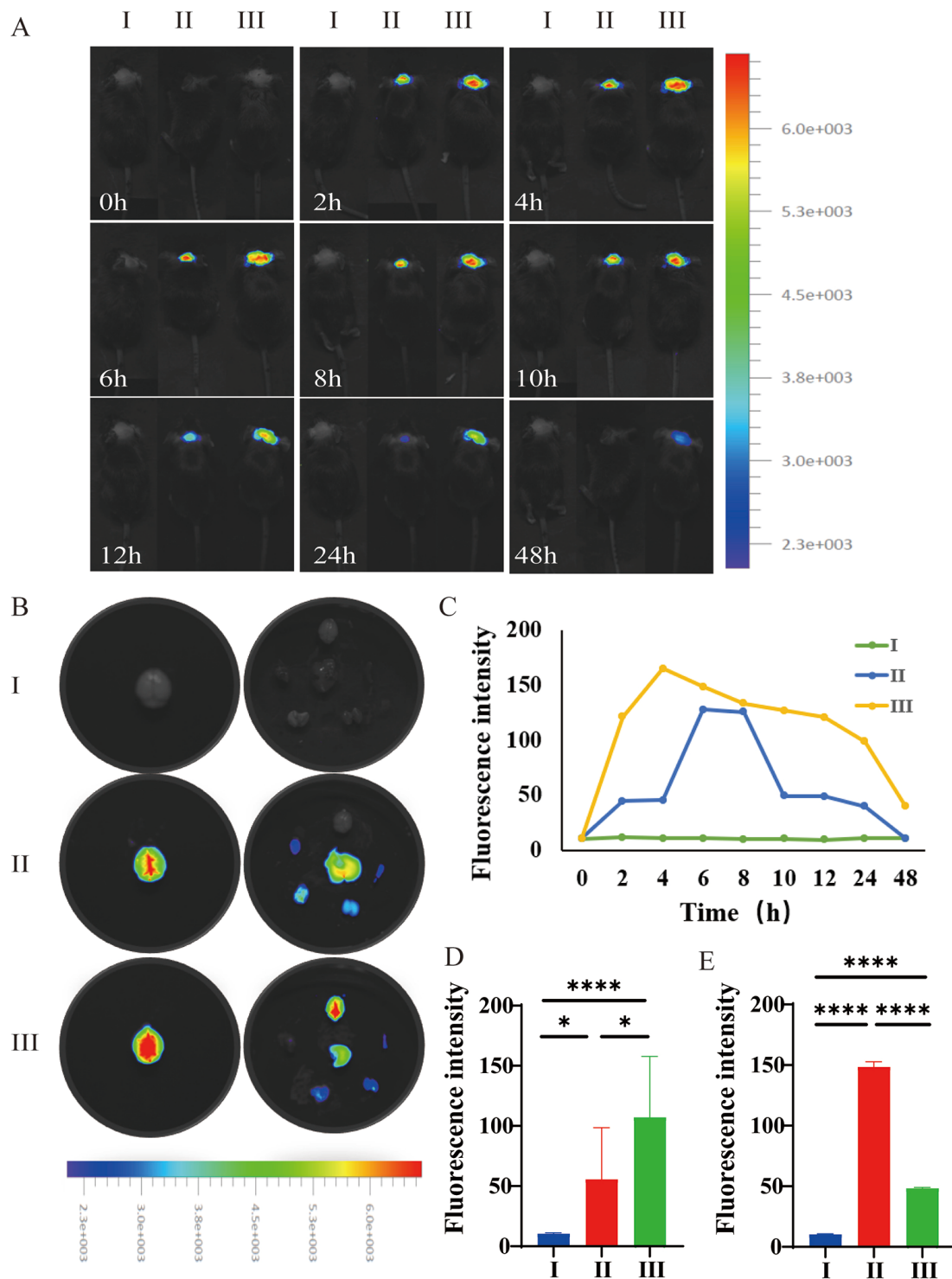


Fig. 10. In vivo biodistribution and brain targeting efficiency of nanoparticles. (A) Real-time fluorescence imaging of Cy5.5-labeled nanoparticles in C57BL/6 neonatal mice after intraperitoneal injection (Groups I: PBS; II: Cy5.5-siC-NPs; and III: Cy5.5-M-R@siC-NPs). Imaging was performed using a chemiluminescence imaging system with excitation/emission wavelengths set to 675/720 nm (Cy5.5 channel). (B) *Ex vivo* fluorescence imaging of major organs (heart, liver, spleen, lung, kidney, and brain) at the fluorescence intensity peak (4–6 hours post-injection). (C) Dynamic changes in brain fluorescence intensity (0–48 hours, region of interest [ROI] quantification, $n=9$). (D) Quantitative analysis of brain fluorescence intensity across groups. (E) Total fluorescence intensity comparison among major organs. Data are presented as mean \pm SD. Statistical analysis: two-way ANOVA with Tukey's post-hoc test for time-dependent trends (C); one-way ANOVA with Tukey's post-hoc test for intergroup differences (D,E). (* $p < 0.05$, **** $p < 0.0001$).

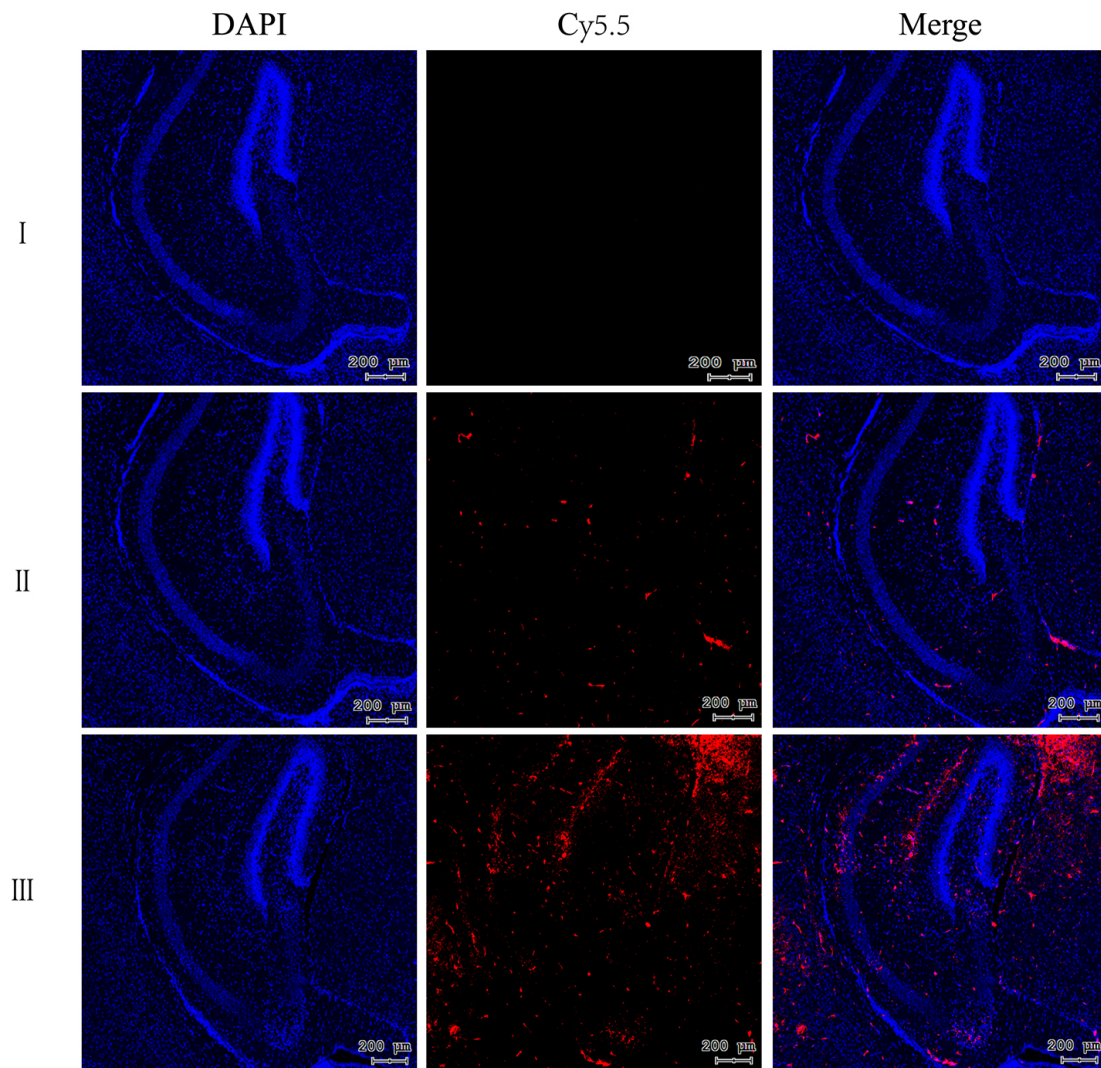


Fig. 11. Fluorescence intensity of Cy5 (red) in the brains of mice in different treatment groups. Scale bar = 200 μm. DAPI (blue) served as nuclear counterstaining. I: PBS-treated group; II: Cy5-siC-NPs-treated group; III: Cy5-M-R@siC-NPs-treated group.

3.8 Animal Experiments to Test the Therapeutic Efficacy of M-R@siC-NPs

3.8.1 Establishment of the HIBD Model

The murine HIBD model was established using the Rice-Vannucci method [53]. Cortical blood flow was quantified using laser speckle flowmetry at 24 hours post-surgery. Compared with those in the sham-operated group, HIBD mice exhibited a statistically significant reduction in left cortical blood flow (Fig. 14A,B), confirming successful model induction.

Post-mortem examination of brain tissues revealed progressive pathological changes. Sham-operated mice displayed normal brain morphology, characterized by a uniform texture, smooth surfaces, and an intact structure. In contrast, the brains of HIBD mice exhibited time-dependent deterioration, including mild cerebral edema at 3 days post-HIBD (indicative of ischemia–hypoxia injury), ipsilateral infarction foci at 5 days (reflecting vascular occlusion and

neuronal necrosis), and exacerbated tissue damage at 7 days, including softening of the brain parenchyma, regional necrosis, and structural disintegration (Fig. 14C). These findings collectively validate the reliability of the HIBD model for studying hypoxic–ischemic brain injury progression.

3.8.2 *In Vivo* Therapeutic Efficacy Evaluation

To build upon our *in vitro* findings, the therapeutic efficacy of M-R@siC-NPs was evaluated in a C57BL/6 HIBD model. The mice were divided into four groups: sham-operated, HIBD, siC-NPs-treated, and M-R@siC-NPs-treated. At 5 days post-treatment, brain tissues were subjected to H&E staining. The brain tissues of sham-operated mice exhibited normal cellular morphology with tightly arranged neurons and no injury. The brain tissues of HIBD mice showed pyknotic nuclei, deep staining, and inflammatory cell infiltration. While the brain tissues of siC-NPs-treated mice displayed reduced injury severity, in-

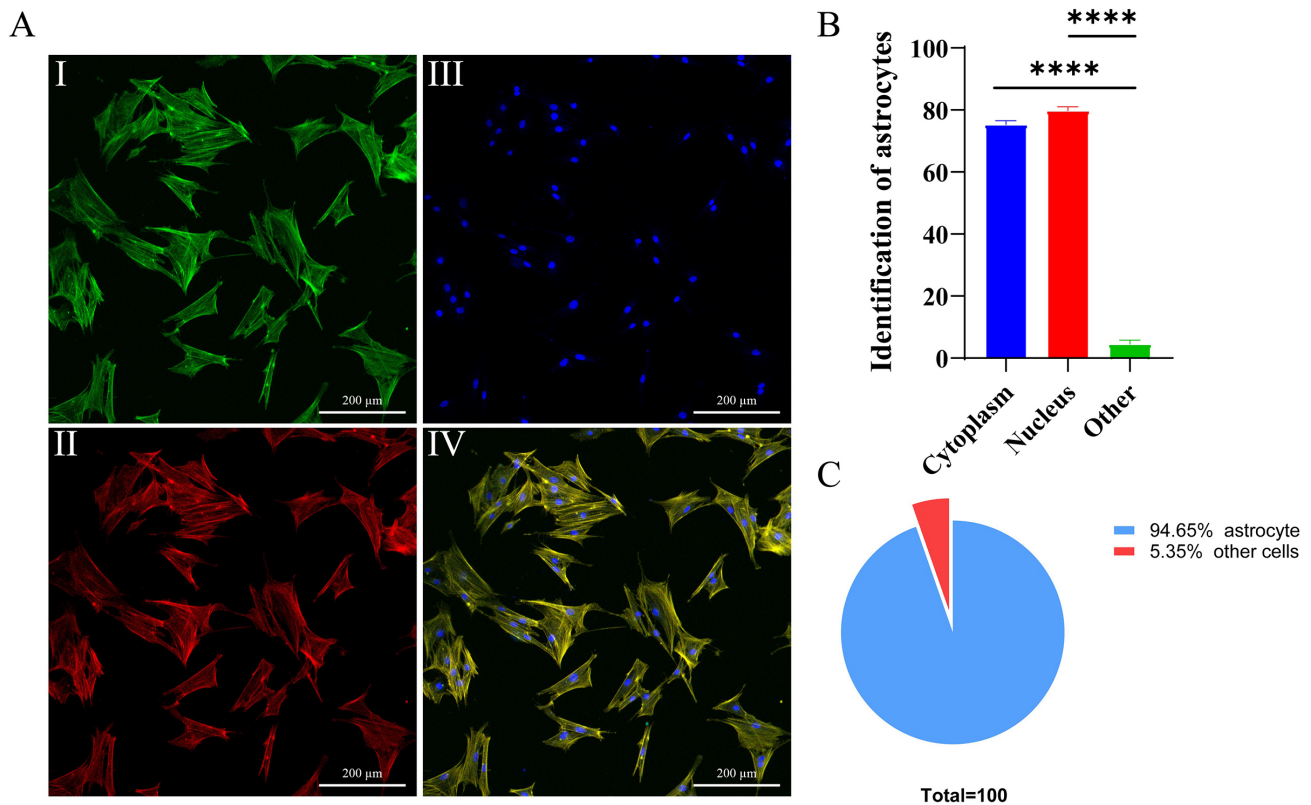


Fig. 12. Morphological characterization and purity analysis of primary astrocytes. (A) Immunofluorescence analysis: A-I: GFAP (astrocyte marker, green); A-II: phalloidin-labeled cytoskeleton (red); A-III: DAPI-stained nuclei (blue); A-IV: merged tri-channel image. (B) Antibodies labeled with GFAP bind to specific proteins in the cytoplasm (not the nucleus) of primary astrocytes, and the proportion of positive cells is observed under a fluorescence microscope, **** $p < 0.0001$. (C) Quantitative analysis confirmed an average purity of 94.65% in the cultures. Scale bar = 200 μm .

cluding decreased inflammatory infiltration and improved edema, the brain tissues of M-R@siC-NPs-treated mice demonstrated significant improvement, including an intact brain architecture, minimal neuronal damage, orderly cellular arrangement, and markedly reduced inflammatory cell infiltration (Fig. 15A).

Immunofluorescence analysis revealed distinct astrocyte activation states across groups (Fig. 15B). Weak GFAP fluorescence in brain tissues from sham-operated mice indicated quiescent astrocytes. In contrast, intense GFAP signals in brain tissues from HIBD mice reflected hypoxia-ischemia-induced astrocyte activation and secondary neuroinflammation. While treatment with siC-NPs reduced the GFAP intensity compared with that in HIBD mice, treatment with M-R@siC-NPs achieved the most pronounced suppression, with significantly weaker GFAP fluorescence than in both the HIBD and siC-NPs-treated groups, underscoring the superior efficacy of targeted nanoparticles for inhibiting astrocyte activation.

Western blot analysis confirmed these trends in an astrocyte activation marker (GFAP) and an inflammatory cytokine (IL-1 β). Compared with the brain tissues of sham-operated mice, those of HIBD mice exhibited upreg-

ulated GFAP and IL-1 β expression, confirming hypoxia-ischemia-driven astrocyte activation and neuroinflammation. Both siC-NPs and M-R@siC-NPs treatment reduced the levels of these proteins, but treatment with M-R@siC-NPs achieved significantly greater suppression (Fig. 15C–E, the original western blot images can be found in the **Supplementary Materials**). Statistical analysis revealed that the GFAP and IL-1 β levels in the M-R@siC-NPs group were markedly lower than those in the HIBD and siC-NPs groups. These findings collectively demonstrate that M-R@siC-NPs effectively alleviate neuroinflammation and suppress astrocyte activation, thereby mitigating brain injury.

3.9 Behavioral Assessments to Investigate the Therapeutic Efficacy of M-R@siC-NPs

3.9.1 Effects of Nanoparticle Treatment on Short-Term Behaviors

The righting reflex test evaluates sensorimotor development by measuring the latency to rightward rotation after placement in a supine position. Sham-operated mice exhibited rapid righting reflexes with significantly shorter latency times compared with HIBD mice (Fig. 16A), which showed prolonged latencies, indicating impaired neuro-

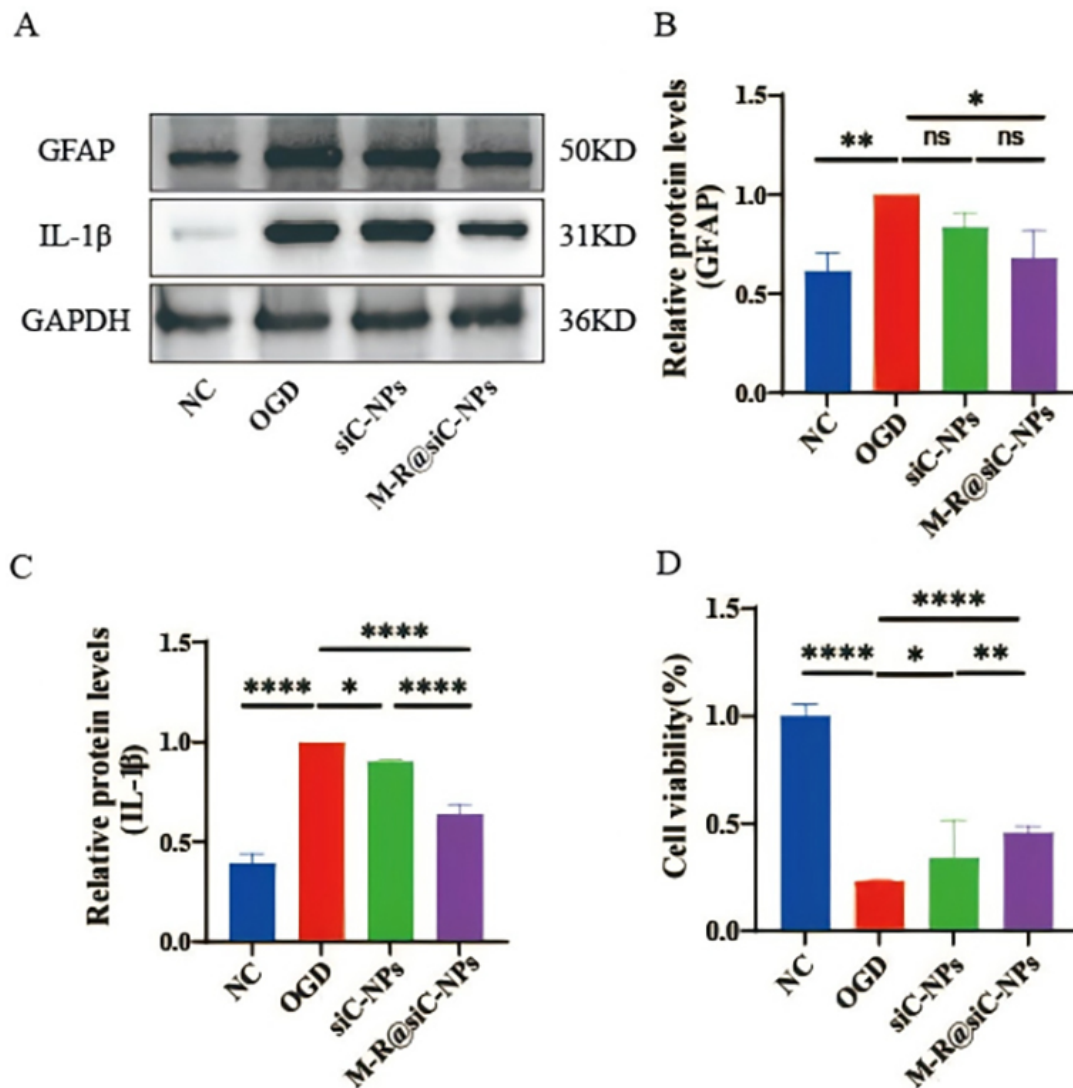


Fig. 13. *In vitro* expression of GFAP and interleukin-1 β (IL-1 β) proteins and cell viability across treatment groups. (A) Western blot analysis of GFAP and IL-1 β protein expression. (B,C) Quantitative analysis of GFAP and IL-1 β protein levels. (D) Cell viability determined by CCK-8 assay. Data are presented as mean \pm SD ($n = 3$). Statistical analysis was performed using one-way ANOVA followed by Tukey's post-hoc test. (ns $p \geq 0.05$; * $p < 0.05$; ** $p < 0.01$; **** $p < 0.0001$).

muscular control and balance due to neurological injury. Treatment with siC-NPs and M-R@siC-NPs reduced latency times, with the M-R@siC-NPs-treated group demonstrating the most marked improvement.

Using the negative geotaxis test, the mice in each group were assessed for their ability to climb upward on an inclined plane. The HIBD mice displayed significantly longer escape latencies than the sham-operated control mice (Fig. 16B), reflecting compromised neuromuscular strength and coordination. While both treatment groups showed improved latencies compared with the HIBD mice, treatment with M-R@siC-NPs led to statistically significant recovery, suggesting enhanced motor function restoration.

3.9.2 Effects of Nanoparticle Treatment on Long-Term Behaviors

To evaluate spatial learning and memory recovery, the Morris water maze test was performed over 5 days (Fig. 16C). During training (days 1–4), sham-operated mice exhibited progressively shorter escape latencies, indicating efficient spatial memory formation. In contrast, the HIBD mice displayed prolonged latencies (Fig. 16D) and disorganized swimming paths, reflecting hippocampal dysfunction. Treatment with siC-NPs or M-R@siC-NPs reduced latency times and increased platform-crossing frequency. Notably, M-R@siC-NPs-treated mice showed the greatest improvements in learning and memory retention during the probe trial (day 5, Fig. 16E).

In the mouse HIBD model, the siC-NPs group exhibited significantly less improvement in brain patholog-

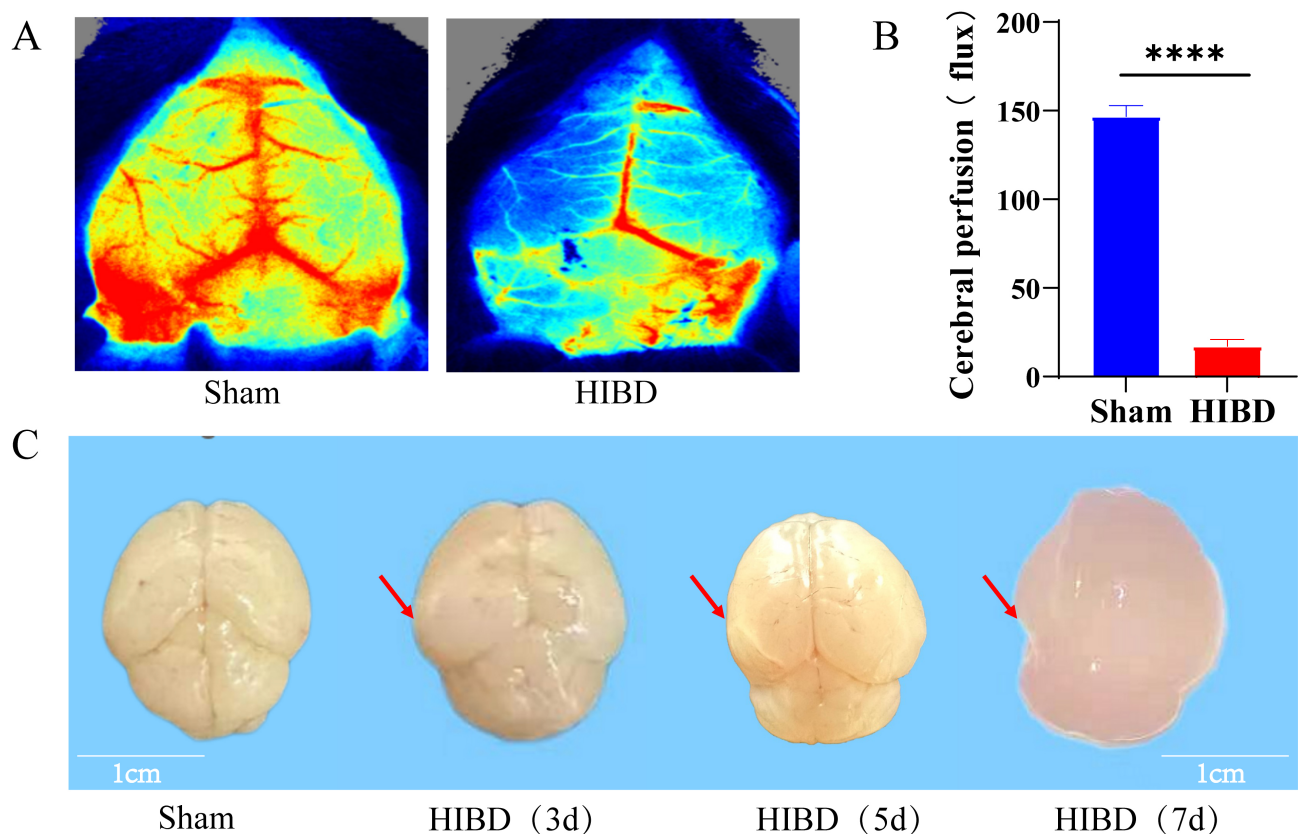


Fig. 14. Cerebral blood flow perfusion and pathological morphological changes in HIBD model mice. (A) Comparative laser speckle flowmetric images of cerebral blood flow in sham-operated and HIBD groups. (B) Quantitative analysis of left cerebral blood flow perfusion. (C) Macroscopic observations of HIBD brain tissues at 3, 5, and 7 days post-surgery (arrows indicate: 3 d edema, 5 d infarction, 7 d tissue softening/loss). Scale bar = 1 cm. Data are presented as mean \pm SD ($n = 6$). Statistical analysis: unpaired t -test for (B); one-way ANOVA for (A,C). (**** $p < 0.0001$). HIBD, hypoxic–ischemic brain damage.

ical lesions and neurological function recovery compared to the M-R@siC-NPs group. Combined with *in vivo* fluorescence imaging results—where the cerebral accumulation of M-R@siC-NPs was 3 times that of siC-NPs—it was further confirmed that the BBB penetration capability and astrocyte-targeting ability, mediated by M-PEG-lipid and DSPE-PEG2000-RVG29, are the key factors underlying the superior *in vivo* therapeutic efficacy of the targeted nanoparticles. Moreover, the presence of siC-NPs clearly verifies that this efficacy advantage originates from the targeted modification, rather than the carrier or siRNA itself.

4. Discussion

Current HIE therapies are associated with multiple limitations. For example, the gold standard approach, hypothermia, can only be employed in neonates within 6 h post-birth, and its use is still associated with 44–53% mortality/severe disability rates and infection risks [7,54–58]. While experimental drugs (allopurinol, melatonin) have shown promise, long-term safety data for these therapeutics are lacking [59–61]. Stem cell therapies encounter ethical/immunological barriers [62,63]. This study success-

fully constructed brain-targeting LNPs (M-R@siC-NPs) for astrocyte-specific delivery of *circHIPK2* siRNA, which exhibited significant therapeutic efficacy in a murine HIBD model. The dual-targeting nanoplateform efficiently traversed the BBB, silenced *circHIPK2* expression, inhibited astrocyte activation, and attenuated neuroinflammation, providing a novel strategy for neonatal HIE therapy (Fig. 17). In contrast with existing therapies, M-R@siC-NPs offer superior targeting, efficacy, and safety. Compared with glioma-targeted liposomes specifically, M-R@siC-NPs exhibit greater siRNA encapsulation and brain accumulation (RVG29-mediated hippocampal targeting), minimizing systemic toxicity.

Neuroinflammation is central to ischemia–reperfusion injury in HIE. During the pathogenesis of HIE, astrocytes undergo aberrant activation, characterized by upregulated GFAP expression and the release of pro-inflammatory mediators (e.g., $\text{TNF-}\alpha$, $\text{IL-1}\beta$), which exacerbates neuronal damage and disease progression [64]. By precisely suppressing astrocyte activation, M-R@siC-NPs effectively disrupted this pathological cascade, offering innovative therapeutic potential. While previous studies have ex-

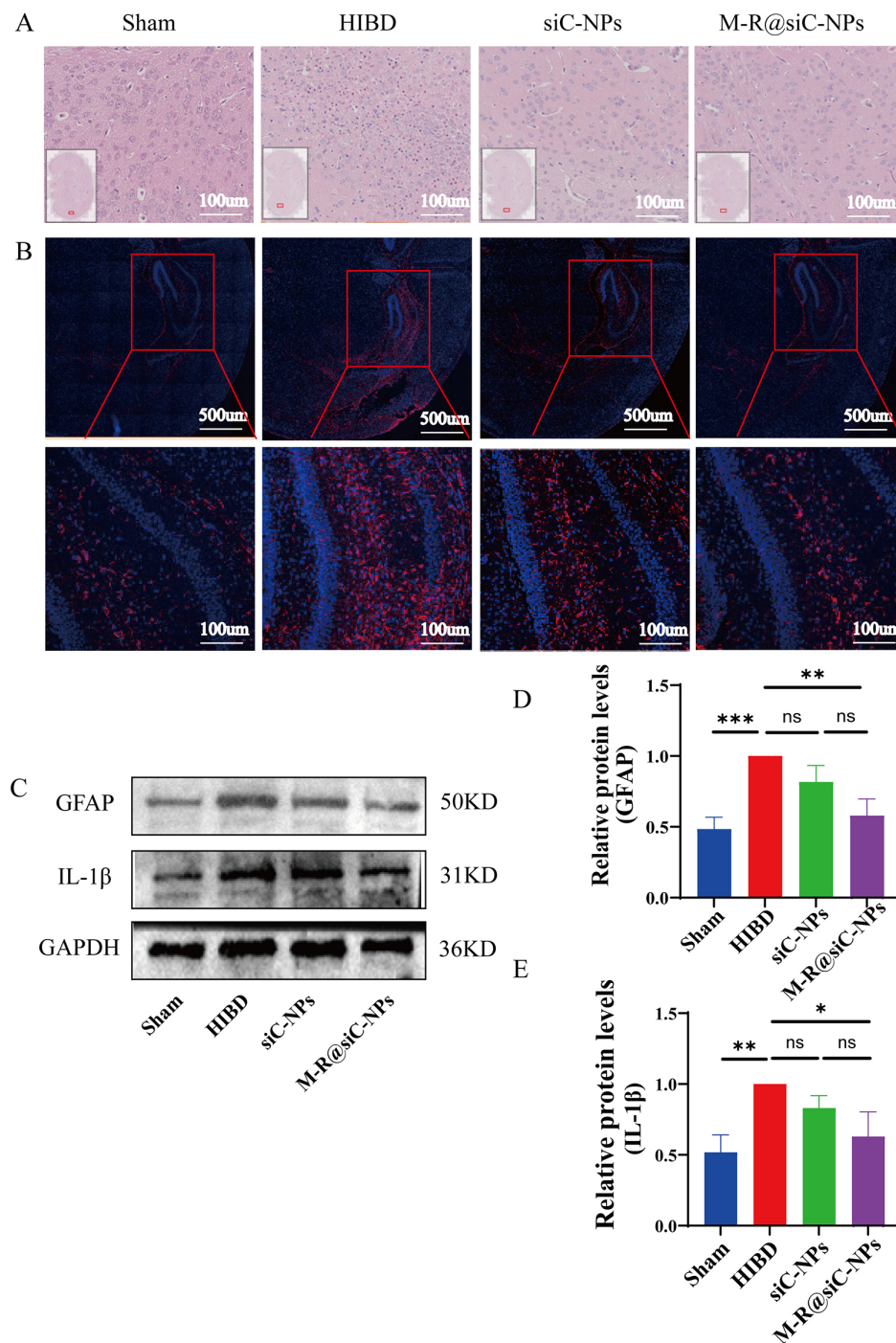


Fig. 15. Histopathological changes and GFAP/IL-1 β protein expression in brain tissues of sham and HIBD mice. (A) H&E staining of brain tissues at 5 days post-treatment (scale bars = 100 μ m). Sham group: neurons exhibited normal morphology with tight arrangement. HIBD model group: pyknotic nuclei, deep staining, and inflammatory cell infiltration. Treatment groups (siC-NPs, and M-R@siC-NPs): Reduced pathological damage compared with HIBD model group. (B) Immunofluorescence analysis of GFAP expression in the hippocampus (red: GFAP; blue: DAPI nuclear staining). Scale bars: 500 μ m (hippocampus) and 100 μ m (cortex). Sham group: weak GFAP fluorescence (quiescent astrocytes). HIBD model group: markedly increased GFAP-positive cells in the cortex and hippocampus (red fluorescence). Treatment groups: reduced GFAP fluorescence intensity, with M-R@siC-NPs showing the greatest level of suppression. (C) Western blot analysis of GFAP and IL-1 β protein expression in brain tissues. (D,E) Quantitative analysis of GFAP and IL-1 β levels. Data are presented as mean \pm SD (n = 3). Statistical analysis: one-way ANOVA followed by Tukey's post-hoc test (ns: $p \geq 0.05$; * $p < 0.05$; ** $p < 0.01$; *** $p < 0.001$).

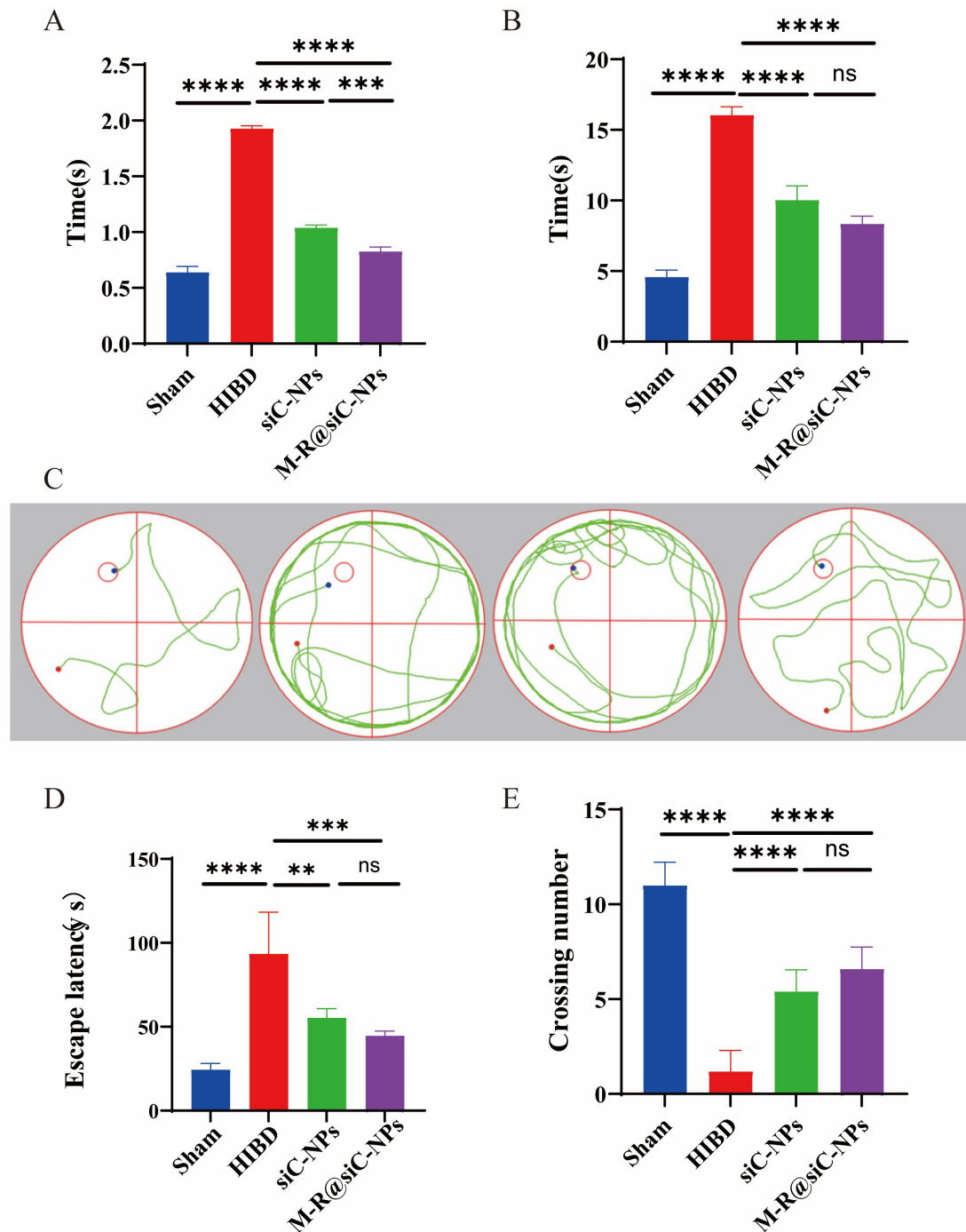


Fig. 16. Therapeutic effects of M-R@siC-NPs on behavioral and cognitive functions in HIBD model mice. (A) Righting reflex test: M-R@siC-NPs treatment significantly shortened latency compared with that in the HIBD model group ($p < 0.0001$). (B) Negative geotaxis test: Improved motor coordination was observed in the treatment group ($p < 0.0001$). (C) Representative swimming trajectories on day 5 of the Morris water maze test (red circle indicates target platform location). (D) Escape latency during acquisition phase: Prolonged latency in HIBD mice was reversed by M-R@siC-NPs treatment. (E) Number of platform crossings on day 5: treatment group showed increased crossings versus HIBD controls. Key observations: HIBD mice exhibited disorganized swimming paths, prolonged escape latency, and reduced platform crossings. M-R@siC-NPs treatment normalized behavioral parameters and spatial memory performance. Data presentation: Values expressed as mean \pm SD ($n = 6$). Statistical analysis: Righting reflex/negative geotaxis: unpaired t -test. Water maze latency: two-way repeated measures ANOVA. Platform crossings: one-way ANOVA; ns $p \geq 0.05$; ** $p < 0.01$, *** $p < 0.001$, **** $p < 0.0001$.

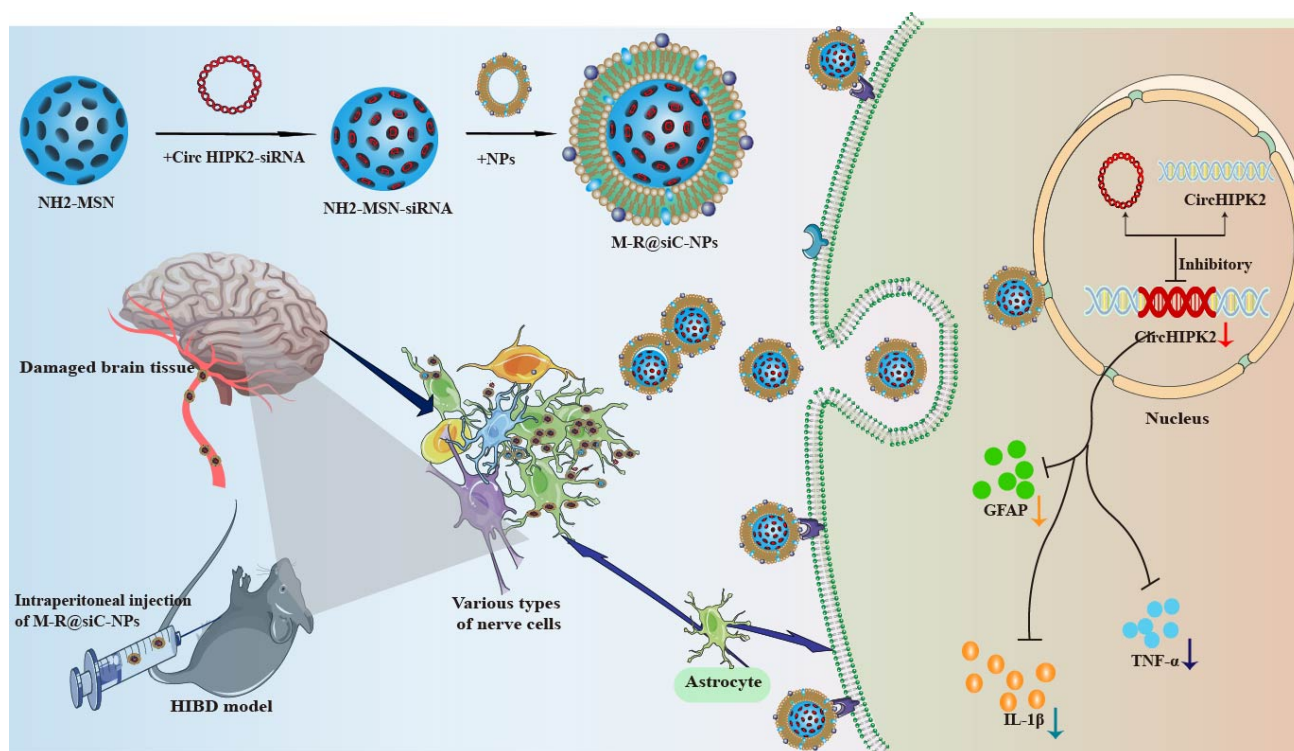


Fig. 17. Schematic illustration of the molecular mechanism by which M-R@siC-NPs alleviate HIBD through a *circHIPK2* silencing-mediated reduction of astrocyte activation. TNF- α , tumor necrosis factor- α . \downarrow indicates decreased expression of *circHIPK2*, GFAP, IL-1 β , and TNF- α . The figure was created using bioRender (<https://www.biorender.com/>).

plored astrocyte modulation, our dual-targeted delivery system introduces unique advancements in carrier design and specificity. Composed of DPPC, cholesterol, DSPE-PEG2000, DSPE-PEG2000-RVG29, and mannose-PEG-lipid, this system involves loading *circHIPK2* siRNA into NH₂-MSNs, forming core-shell LNPs (Fig. 17).

The BBB poses a critical barrier to CNS drug delivery, limiting cerebral bioavailability while increasing systemic toxicity [65,66]. Although RNA interference holds promise, the application of siRNA as therapeutic agents has faced limitations including poor membrane permeability, rapid degradation, mononuclear phagocyte system clearance, renal excretion, and off-target effects [67,68]. To address these limitations, we developed M-R@siC-NPs incorporating MSNs. MSNs exhibit exceptional drug-loading capacity due to their ordered mesopores, high surface area, and modifiable silanol groups [34,69–74]. In this study, positively charged NH₂-MSNs achieved high siRNA loading via electrostatic interactions with negatively charged siRNA.

Liposomes, with their amphiphilic lipid bilayer structure, enable co-delivery of hydrophilic/hydrophobic agents while enhancing BBB penetration [75,76]. Targeted modifications using ligands (e.g., polymers, peptides) further improve brain delivery [38,77]. M-R@siC-NPs were functionalized with a Glucose Transporter 1 (GLUT1)-targeting M-PEG-lipid and the BBB-penetrating DSPE-PEG2000-

RVG29. RVG29 mediates BBB transcytosis via receptor recognition, while M-PEG-lipid directs astrocyte targeting, conferring superior specificity compared with non-targeted siC-NPs.

Cellular uptake of nanoparticles is influenced by the physicochemical properties of the nanoparticles, such as surface charge and size [78–81]. While sub-100 nm particles are better able to penetrate the BBB, 100–150-nm particles exhibit prolonged circulation. However, even larger particles (>250 nm) undergo rapid clearance [82–84]. Positively charged nanoparticles offer good cellular adhesion via electrostatic interactions [85]. Moreover, PEGylation can reduce aggregation, prolonged circulation, and minimize mononuclear phagocyte system-mediated clearance [86–89]. Based on these effects of nanoparticle size and properties, the M-R@siC-NPs developed in this study were optimized to 130–140 nm in diameter (Malvern Nano analysis) with a narrow polydispersity and ability to remain stable for more than 14 days.

The assessment of “nanorisk” requires a comprehensive evaluation of nanoparticle trafficking dynamics, organ-specific accumulation patterns, and toxicity mechanisms in biological systems [90]. Safety assessments in the present study revealed that after treatment with M-R@siC-NPs at concentrations of 20–80 μ g/mL, >90% of astrocytes remained viable (CCK-8 assay), negligible hemolysis occurred, and hematological/biochemical indices were nor-

mal. Histopathological analysis confirmed the absence of organ toxicity after M-R@siC-NPs treatment.

Activated astrocytes critically regulate sterile inflammation and IL-1 β release in HIE [17,91–93]. Previous studies have demonstrated that *circHIPK2* inhibits astrocyte activation and alleviates neuroinflammation through multiple mechanistic pathways [24,25,94]. The experiments in the present study provided evidence that the developed M-R@siC-NPs effectively silenced *circHIPK2* *in vitro* and *in vivo*, suppressing GFAP/IL-1 β expression and improving cell viability. In HIBD model mice, treatment with M-R@siC-NPs reduced neuroinflammation and restored spatial learning/memory (shortened Morris water maze latency; prolonged target quadrant duration). The dual RVG29/mannose-based targeting showed greater efficacy than previous mono-targeted approaches. Mechanistically, *circHIPK2* inhibition may preserve hippocampal synaptic plasticity by attenuating IL-1 β -driven inflammation. In the present study, the HIBD model exhibited a dynamic pattern of macroscopic pathological changes, specifically edema at 3 days, infarction at 5 days, tissue lysis at 7 days, which is highly consistent with the classic findings of neonatal HIBD model studies in the field. The Rice-Vannucci method for establishing HIBD models, first developed by Rice *et al.* [95], has clearly demonstrated a consistent pathological sequence in the ischemic cerebral hemisphere of neonatal rats: edema at 3 days post-surgery, infarction formation at 5 days, and tissue necrosis at 7 days. This model and its associated pathological characteristics have become a consensus in the field, laying a critical foundation for subsequent research [95]. Additionally, studies on neonatal mouse HIBD models have further confirmed that the ischemic cerebral hemisphere exhibits localized tissue loss at 7 days post-surgery due to infarct expansion, and this change shows a significant negative correlation with the reduction in cerebral blood flow ($r = -0.87$, $p < 0.001$) [96]. Motor coordination improvements (righting reflex/negative geotaxis tests) suggest cerebellar–vestibular pathway repair, although the long-term cognitive effects require further evaluation.

Currently, the treatment of HIBD primarily relies on two major strategies: neuronal protection and broad-spectrum anti-inflammation, both of which have significant limitations. On one hand, neurons exhibit extremely poor tolerance to hypoxia-ischemia—intracellular ATP depletion exceeds 80% within 2 hours of ischemia. Traditional neurotrophic factors such as brain-derived neurotrophic factor (BDNF) can only delay neuronal apoptosis by approximately 15%–20% due to restricted BBB permeability and downregulation of target receptors. Although antioxidants like N-acetylcysteine can temporarily reduce oxidative stress, they fail to block cascading necrosis via the mitochondrial pathway; clinical translation trials have shown that their 90-day neurological function improvement rate is only 5.7% [97–99]. On the other hand, while broad-

spectrum anti-inflammatory strategies can inhibit early pro-inflammatory factors IL-1 β and TNF- α , they simultaneously disrupt late-stage reparative inflammation, such as M2 microglial polarization, leading to a 50% reduction in neural stem cell proliferation ($p < 0.01$) and significant delays in the recovery of motor and cognitive functions [100].

As core regulators of CNS homeostasis, astrocytes play a crucial role in HIBD. They clear over 80% of glutamate in the synaptic cleft by highly expressing glutamine synthetase (GS), thereby inhibiting excitotoxicity; secrete IL-6 and C-X-C motif chemokine ligand 12 (CXCL12) to regulate neuroinflammation; and maintain BBB integrity through the modulation of vascular endothelial growth factor (VEGF) and TGF- β [101]. However, traditional intervention methods mostly involve non-specific inhibition—for example, the pan-glial inhibitor minocycline. While suppressing the excessive activation of astrocytes, it non-selectively impairs the functions of normal glial cells, resulting in a 60% reduction in hippocampal neurogenesis in the late stage ($p < 0.001$) and a 40% prolongation of escape latency in the Morris water maze test [102].

In this study, a novel mannose/RVG29 peptide dual-modified lipid nanoparticle M-R@siC-NPs was innovatively constructed to overcome the bottlenecks of traditional interventions. Leveraging the high expression of mannose receptors (MR) on the surface of astrocytes, the mannose modification enables specific endocytosis of the nanoparticles; combined with the RVG29 peptide, which enhances brain penetration capability, this system can efficiently deliver *circHIPK2* siRNA into astrocytes. M-R@siC-NPs demonstrate great potential in inhibiting astrocyte activation, exerting anti-inflammatory effects, and alleviating HIBD-induced brain damage, holding promise as an innovative strategy for the treatment of HIE.

The present study has some limitations that must be considered and addressed in future research. The sample size in this study was small, and the long-term biodistribution and toxicity of M-R@siC-NPs were not evaluated. Moreover, the mechanisms by which M-R@siC-NPs interact with the BBB remain unclear. Future work should include expanded cohorts, assessment of scale-up feasibility, proteomics analyses for pathway elucidation, and *in vivo* imaging to visualize BBB traversal.

5. Conclusions

In conclusion, this study successfully developed M-R@siC-NPs with dual functions based on the inclusion of RVG29 peptide and mannose-PEG-lipid, offering good BBB penetration and astrocyte-targeting efficiency. These nanoparticles achieved efficient *circHIPK2* silencing while exhibiting excellent stability and biosafety. Mechanistically, the results of this study indicate that M-R@siC-NPs reduce astrocyte activation and mitigate neuroinflammation, effectively ameliorating brain injury in HIBD model mice. This work not only establishes a novel RNA

interference-based targeted therapy for neuroinflammation but also provides a foundation for the clinical translation of *circHIPK2* as a therapeutic target in HIE. Overall, M-R@siC-NPs represent a breakthrough in HIE therapy, combining BBB penetration, astrocyte specificity, and robust siRNA delivery. This dual-targeted system overcomes multiple limitations of conventional treatments, demonstrating transformative potential for precision gene therapy in neonatal brain injury.

Abbreviations

WB, Western blot; qRT-PCR, Quantitative reverse transcription polymerase chain reaction; CCK-8, Cell counting kit-8; CREA, Creatinine; CNS, Central nervous system; PEG, Polyethylene glycol; BBB, Blood-brain barrier; GLUT1, Glucose transporter 1; HIBD, Hypoxic-ischemic brain damage; HIE, Hypoxic-ischemic encephalopathy; GFAP, Glial fibrillary acidic protein; NP, Nanoparticle; OGD, Oxygen-glucose deprivation; PBS, Phosphate-buffered saline; PLT, Platelet; ALB, Albumin; ALT, Alanine transaminase; AST, Aspartate transaminase; RVG, Rabies virus glycoprotein; siRNA, Small interfering RNA; IL-1 β , Interleukin-1 β ; HGB, Hemoglobin; RBC, Red blood cell; WBC, White blood cell; TBIL, Total bilirubin; GLUT1, Glucose Transporter 1; CXCL12, C-X-C motif chemokine ligand 12; VEGF, vascular endothelial growth factor.

Availability of Data and Materials

The data that support the findings of this study are available from the corresponding author upon reasonable request.

Author Contributions

YXD, FHS, SXW, YTZ and XL designed the research study. YXD, DYQ, DF and YJS performed the research. ZHC and RCM provided help and advice on the WB experiments. DYQ, DF and YJS provided help and advice on the H&E experiments. YXD and FHS analyzed the data. YTZ and FW demonstrated outstanding efforts in critical revision of the article and grant preparation. ZHC, RCM, DYQ, DF, YJS, and FW have actively participated in the conception or design of the research, as well as the acquisition, analysis, and interpretation of the study data. All authors contributed to editorial changes in the manuscript. All authors read and approved the final manuscript. All authors have participated sufficiently in the work and agreed to be accountable for all aspects of the work. All authors have read and approved the final manuscript for publication.

Ethics Approval and Consent to Participate

All animal experiments were approved by the Ethics Committee of the Second Hospital of Lanzhou University (Approval No. D2024-439) and were performed in

strict accordance with the Regulations on the Administration of Laboratory Animals and the international standards for the care and use of laboratory animals established by AAALAC.

Acknowledgment

We would like to thank the Second Hospital of Lanzhou University for providing the experimental site for this study. Additionally, we appreciate Medjaden, Inc. for offering scientific editing services for this manuscript.

Funding

This research received no external funding.

Conflict of Interest

The authors declare no conflict of interest.

Supplementary Material

Supplementary material associated with this article can be found, in the online version, at <https://doi.org/10.31083/JIN45212>.

References

- [1] Greco P, Nencini G, Piva I, Scioscia M, Volta CA, Spadaro S, *et al.* Pathophysiology of hypoxic-ischemic encephalopathy: a review of the past and a view on the future. *Acta Neurologica Belgica*. 2020; 120: 277–288. <https://doi.org/10.1007/s13760-020-01308-3>.
- [2] Vega-Del-Val C, Arnaez J, Caserio S, Gutiérrez EP, Benito M, Castañón L, *et al.* Temporal Trends in the Severity and Mortality of Neonatal Hypoxic-Ischemic Encephalopathy in the Era of Hypothermia. *Neonatology*. 2021; 118: 685–692. <https://doi.org/10.1159/000518654>.
- [3] Disdier C, Stonestreet BS. Hypoxic-ischemic-related cerebrovascular changes and potential therapeutic strategies in the neonatal brain. *Journal of Neuroscience Research*. 2020; 98: 1468–1484. <https://doi.org/10.1002/jnr.24590>.
- [4] Finder M, Boylan GB, Twomey D, Ahearn C, Murray DM, Hallberg B. Two-Year Neurodevelopmental Outcomes After Mild Hypoxic Ischemic Encephalopathy in the Era of Therapeutic Hypothermia. *JAMA Pediatrics*. 2020; 174: 48–55. <https://doi.org/10.1001/jamapediatrics.2019.4011>.
- [5] Wei KL, Liu SJ, Zhong BM. Early Management of High-Risk Neonates (pp. 287–295). Science Press: Beijing. 2020.
- [6] Chen LJ, Xu JL, Zhao W. *Pediatrics* (pp. 83–87). 2nd edn. China University of Science and Technology Press: Hefei. 2017.
- [7] Subspecialty Group of Neonatology, the Society of Pediatrics, Chinese Medical Association, Editorial Board, Chinese Journal of Pediatrics. Expert consensus on therapeutic hypothermia in neonates with hypoxic ischemic encephalopathy (2022). *Zhonghua Er Ke Za Zhi = Chinese Journal of Pediatrics*. 2022; 60: 983–989. <https://doi.org/10.3760/cma.j.cn.112140-20220418-00344>.
- [8] Serrenho I, Rosado M, Dinis A, M Cardoso C, Grãos M, Manadas B, *et al.* Stem Cell Therapy for Neonatal Hypoxic-Ischemic Encephalopathy: A Systematic Review of Preclinical Studies. *International Journal of Molecular Sciences*. 2021; 22: 3142. <https://doi.org/10.3390/ijms22063142>.
- [9] Saunders NR, Ek CJ, Habgood MD, Dziegielewska KM. Barri-

- ers in the brain: a renaissance? *Trends in Neurosciences*. 2008; 31: 279–286. <https://doi.org/10.1016/j.tins.2008.03.003>.
- [10] Liu F, McCullough LD. Inflammatory responses in hypoxic ischemic encephalopathy. *Acta Pharmacologica Sinica*. 2013; 34: 1121–1130. <https://doi.org/10.1038/aps.2013.89>.
 - [11] Araya R, Kudo M, Kawano M, Ishii K, Hashikawa T, Iwasato T, *et al.* BMP signaling through BMPRIA in astrocytes is essential for proper cerebral angiogenesis and formation of the blood-brain-barrier. *Molecular and Cellular Neurosciences*. 2008; 38: 417–430. <https://doi.org/10.1016/j.mcn.2008.04.003>.
 - [12] Ahmad SR, Zeyauallah M, AlShahrani AM, Dawria A, Ali H, Mohieldin A, *et al.* Deciphering the Enigma of Neuron-Glial Interactions in Neurological Disorders. *Frontiers in bioscience (Landmark edition)*. 2024; 29: 142. <https://doi.org/10.31083/j.fbl2904142>.
 - [13] Cavaliere G, Traina G. Neuroinflammation in the Brain and Role of Intestinal Microbiota: An Overview of the Players. *Journal of integrative neuroscience*. 2023; 22: 148. <https://doi.org/10.31083/j.jin2206148>.
 - [14] Liao RJ, Jiang L, Wang RR, Zhao HW, Chen Y, Li Y, *et al.* Histidine provides long-term neuroprotection after cerebral ischemia through promoting astrocyte migration. *Scientific Reports*. 2015; 5: 15356. <https://doi.org/10.1038/srep15356>.
 - [15] Liddelow SA, Barres BA. Regeneration: Not everything is scary about a glial scar. *Nature*. 2016; 532: 182–183. <https://doi.org/10.1038/nature17318>.
 - [16] Seifert G, Schilling K, Steinhäuser C. Astrocyte dysfunction in neurological disorders: a molecular perspective. *Nature Reviews. Neuroscience*. 2006; 7: 194–206. <https://doi.org/10.1038/nrn1870>.
 - [17] Villapol S, Gelot A, Renolleau S, Charriat-Marlangue C. Astrocyte responses after neonatal ischemia: the yin and the yang. *The Neuroscientist: a Review Journal Bringing Neurobiology, Neurology and Psychiatry*. 2008; 14: 339–344. <https://doi.org/10.1177/1073858408316003>.
 - [18] Rossi DJ, Brady JD, Mohr C. Astrocyte metabolism and signaling during brain ischemia. *Nature Neuroscience*. 2007; 10: 1377–1386. <https://doi.org/10.1038/nn2004>.
 - [19] Takata F, Nakagawa S, Matsumoto J, Dohgu S. Blood-Brain Barrier Dysfunction Amplifies the Development of Neuroinflammation: Understanding of Cellular Events in Brain Microvascular Endothelial Cells for Prevention and Treatment of BBB Dysfunction. *Frontiers in cellular neuroscience*. 2021; 15: 661838. <https://doi.org/10.3389/fncel.2021.661838>.
 - [20] Brekke E, Berger HR, Widerøe M, Sonnewald U, Morken TS. Glucose and Intermediary Metabolism and Astrocyte-Neuron Interactions Following Neonatal Hypoxia-Ischemia in Rat. *Neurochemical Research*. 2017; 42: 115–132. <https://doi.org/10.1007/s11064-016-2149-9>.
 - [21] Bustelo M, Barkhuizen M, van den Hove DLA, Steinbusch HWM, Bruno MA, Loidl CF, *et al.* Clinical Implications of Epigenetic Dysregulation in Perinatal Hypoxic-Ischemic Brain Damage. *Frontiers in Neurology*. 2020; 11: 483. <https://doi.org/10.3389/fneur.2020.00483>.
 - [22] Rybak-Wolf A, Stottmeister C, Glažar P, Jens M, Pino N, Giusti S, *et al.* Circular RNAs in the Mammalian Brain Are Highly Abundant, Conserved, and Dynamically Expressed. *Molecular Cell*. 2015; 58: 870–885. <https://doi.org/10.1016/j.molcel.2015.03.027>.
 - [23] Venø MT, Hansen TB, Venø ST, Clausen BH, Grebing M, Finsen B, *et al.* Spatio-temporal regulation of circular RNA expression during porcine embryonic brain development. *Genome Biology*. 2015; 16: 245. <https://doi.org/10.1186/s13059-015-0801-3>.
 - [24] Huang R, Zhang Y, Han B, Bai Y, Zhou R, Gan G, *et al.* Circular RNA HIPK2 regulates astrocyte activation via cooperation of autophagy and ER stress by targeting MIR124-2HG. *Autophagy*. 2017; 13: 1722–1741. <https://doi.org/10.1080/15548627.2017.1356975>.
 - [25] Huang R, Cai L, Ma X, Shen K. Autophagy-mediated circHIPK2 promotes lipopolysaccharide-induced astrocytic inflammation via SIGMAR1. *International Immunopharmacology*. 2023; 117: 109907. <https://doi.org/10.1016/j.intimp.2023.109907>.
 - [26] Pardridge WM. The blood-brain barrier: bottleneck in brain drug development. *NeuroRx: the Journal of the American Society for Experimental NeuroTherapeutics*. 2005; 2: 3–14. <https://doi.org/10.1602/neurorx.2.1.3>.
 - [27] Abbott NJ, Patabendige AAK, Dolman DEM, Yusof SR, Begley DJ. Structure and function of the blood-brain barrier. *Neurobiology of Disease*. 2010; 37: 13–25. <https://doi.org/10.1016/j.nbd.2009.07.030>.
 - [28] Saraiva C, Praça C, Ferreira R, Santos T, Ferreira L, Bernardino L. Nanoparticle-mediated brain drug delivery: Overcoming blood-brain barrier to treat neurodegenerative diseases. *Journal of Controlled Release: Official Journal of the Controlled Release Society*. 2016; 235: 34–47. <https://doi.org/10.1016/j.jconrel.2016.05.044>.
 - [29] Xiao W, Jiang W, Chen Z, Huang Y, Mao J, Zheng W, *et al.* Advance in peptide-based drug development: delivery platforms, therapeutics and vaccines. *Signal Transduction and Targeted Therapy*. 2025; 10: 74. <https://doi.org/10.1038/s41392-024-02107-5>.
 - [30] Delalande A, Bastié C, Pigeon L, Manta S, Lebertre M, Mignet N, *et al.* Cationic gas-filled microbubbles for ultrasound-based nucleic acids delivery. *Bioscience Reports*. 2017; 37: BSR20160619. <https://doi.org/10.1042/BSR20160619>.
 - [31] Oba M, Aoyagi K, Miyata K, Matsumoto Y, Itaka K, Nishiyama N, *et al.* Polyplex micelles with cyclic RGD peptide ligands and disulfide cross-links directing to the enhanced transfection via controlled intracellular trafficking. *Molecular Pharmaceutics*. 2008; 5: 1080–1092. <https://doi.org/10.1021/mp800070s>.
 - [32] Xiao N, Liu J, Liao L, Sun J, Jin W, Shu X. Ultrasound Combined With Microbubbles Increase the Delivery of Doxorubicin by Reducing the Interstitial Fluid Pressure. *Ultrasound Quarterly*. 2019; 35: 103–109. <https://doi.org/10.1097/RUQ.0000000000000381>.
 - [33] Yonezawa S, Koide H, Asai T. Recent advances in siRNA delivery mediated by lipid-based nanoparticles. *Advanced Drug Delivery Reviews*. 2020; 154–155: 64–78. <https://doi.org/10.1016/j.addr.2020.07.022>.
 - [34] Kankala RK, Han YH, Na J, Lee CH, Sun Z, Wang SB, *et al.* Nanoarchitected Structure and Surface Biofunctionality of Mesoporous Silica Nanoparticles. *Advanced Materials (Deerfield Beach, Fla.)*. 2020; 32: e1907035. <https://doi.org/10.1002/adma.201907035>.
 - [35] Kankala RK, Han YH, Xia HY, Wang SB, Chen AZ. Nanoarchitected prototypes of mesoporous silica nanoparticles for innovative biomedical applications. *Journal of Nanobiotechnology*. 2022; 20: 126. <https://doi.org/10.1186/s12951-022-01315-x>.
 - [36] Xu B, Li S, Shi R, Liu H. Multifunctional mesoporous silica nanoparticles for biomedical applications. *Signal Transduction and Targeted Therapy*. 2023; 8: 435. <https://doi.org/10.1038/s41392-023-01654-7>.
 - [37] Vivero-Escoto JL, Slowing IL, Trewyn BG, Lin VSY. Mesoporous silica nanoparticles for intracellular controlled drug delivery. *Small (Weinheim an Der Bergstrasse, Germany)*. 2010; 6: 1952–1967. <https://doi.org/10.1002/smll.200901789>.
 - [38] Antimisariis SG, Marazioti A, Kannavou M, Natsaridis E, Gkartziou F, Kogkos G, *et al.* Overcoming barriers by local drug delivery with liposomes. *Advanced Drug Delivery Reviews*. 2021; 174: 53–86. <https://doi.org/10.1016/j.addr.2021.01.019>.
 - [39] Kim YK. RNA Therapy: Current Status and Future Potential. *Chonnam Medical Journal*. 2020; 56: 87–93. <https://doi.org/10.4062/cmj.2020.56.1.87>.

- [40] DeLong R. Ushering in a new era of RNA-based therapies. *Communications Biology*. 2021; 4: 577. <https://doi.org/10.1038/s42003-021-02150-w>.
- [41] Khare P, Edgecomb SX, Hamadani CM, Tanner EEL, S Manickam D. Lipid nanoparticle-mediated drug delivery to the brain. *Advanced Drug Delivery Reviews*. 2023; 197: 114861. <https://doi.org/10.1016/j.addr.2023.114861>.
- [42] Kuang J, Rao ZY, Zheng DW, Kuang D, Huang QX, Pan T, *et al.* Nanoparticles Hitchhike on Monocytes for Glioblastoma Treatment after Low-Dose Radiotherapy. *ACS Nano*. 2023; 17: 13333–13347. <https://doi.org/10.1021/acsnano.3c01428>.
- [43] Zha S, Liu H, Li H, Li H, Wong KL, All AH. Functionalized Nanomaterials Capable of Crossing the Blood-Brain Barrier. *ACS Nano*. 2024; 18: 1820–1845. <https://doi.org/10.1021/acsnano.3c10674>.
- [44] Zhang L, Wu T, Shan Y, Li G, Ni X, Chen X, *et al.* Therapeutic reversal of Huntington's disease by in vivo self-assembled siRNAs. *Brain: a Journal of Neurology*. 2021; 144: 3421–3435. <https://doi.org/10.1093/brain/awab354>.
- [45] Peddinti V, Rout B, Agnihotri TG, Gomte SS, Jain A. Functionalized liposomes: an enticing nanocarrier for management of glioma. *Journal of liposome research* vol. 2024; 34: 349–367. <https://doi.org/10.1080/08982104.2023.2270060>.
- [46] Zhang Y, He J, Shen L, Wang T, Yang J, Li Y, *et al.* Brain-targeted delivery of obidoxime, using aptamer-modified liposomes, for detoxification of organophosphorus compounds. *Journal of Controlled Release: Official Journal of the Controlled Release Society*. 2021; 329: 1117–1128. <https://doi.org/10.1016/j.jconrel.2020.10.039>.
- [47] Kucharz K, Kristensen K, Johnsen KB, Lund MA, Lønstrup M, Moos T, *et al.* Post-capillary venules are the key locus for transcytosis-mediated brain delivery of therapeutic nanoparticles. *Nature Communications*. 2021; 12: 4121. <https://doi.org/10.1038/s41467-021-24323-1>.
- [48] Arora S, Sharma D, Singh J. GLUT-1: An Effective Target To Deliver Brain-Derived Neurotrophic Factor Gene Across the Blood Brain Barrier. *ACS Chemical Neuroscience*. 2020; 11: 1620–1633. <https://doi.org/10.1021/acscchemneuro.0c00076>.
- [49] Lei T, Yang Z, Jiang C, Wang X, Yang W, Yang X, *et al.* Mannose-Integrated Nanoparticle Hitchhike Glucose Transporter 1 Recycling to Overcome Various Barriers of Oral Delivery for Alzheimer's Disease Therapy. *ACS Nano*. 2024; 18: 3234–3250. <https://doi.org/10.1021/acsnano.3c09715>.
- [50] Régnier-Vigouroux A. The mannose receptor in the brain. *International Review of Cytology*. 2003; 226: 321–342. [https://doi.org/10.1016/s0074-7696\(03\)01006-4](https://doi.org/10.1016/s0074-7696(03)01006-4).
- [51] van der Zande HJP, Nitsche D, Schlautmann L, Guigas B, Burgdorf S. The Mannose Receptor: From Endocytic Receptor and Biomarker to Regulator of (Meta)Inflammation. *Frontiers in Immunology*. 2021; 12: 765034. <https://doi.org/10.3389/fimmu.2021.765034>.
- [52] Refaat A, Yap ML, Pietersz G, Walsh APG, Zeller J, Del Rosal B, *et al.* In vivo fluorescence imaging: success in preclinical imaging paves the way for clinical applications. *Journal of Nanobiotechnology*. 2022; 20: 450. <https://doi.org/10.1186/s12951-022-01648-7>.
- [53] Vannucci RC, Vannucci SJ. Perinatal hypoxic-ischemic brain damage: evolution of an animal model. *Developmental Neuroscience*. 2005; 27: 81–86. <https://doi.org/10.1159/000085978>.
- [54] Shankaran S, Laptok AR, Ehrenkranz RA, Tyson JE, McDonald SA, Donovan EF, *et al.* Whole-body hypothermia for neonates with hypoxic-ischemic encephalopathy. *The New England Journal of Medicine*. 2005; 353: 1574–1584. <https://doi.org/10.1056/NEJMcp050929>.
- [55] Shah M, Sakr M, Balasundaram P. Neonatal Therapeutic Hypothermia. In: StatPearls [Internet]. StatPearls Publishing: Treasure Island (FL). 2025.
- [56] Azzopardi DV, Strohm B, Edwards AD, Dyet L, Halliday HL, Juszczak E, *et al.* Moderate hypothermia to treat perinatal asphyxial encephalopathy. *The New England Journal of Medicine*. 2009; 361: 1349–1358. <https://doi.org/10.1056/NEJMoa0900854>.
- [57] Roca-LLabrés P, Fontalvo-Acosta M, Aldecoa-Bilbao V, Alarcón A. Therapeutic hypothermia in preterm infants under 36 weeks: Case series on outcomes and brain MRI findings. *European Journal of Pediatrics*. 2025; 184: 113. <https://doi.org/10.1007/s00431-024-05948-y>.
- [58] Wu YW, Monsell SE, Glass HC, Wisnowski JL, Mathur AM, McKinstry RC, *et al.* How well does neonatal neuroimaging correlate with neurodevelopmental outcomes in infants with hypoxic-ischemic encephalopathy? *Pediatric Research*. 2023; 94: 1018–1025. <https://doi.org/10.1038/s41390-023-02510-8>.
- [59] Engel C, Rüdiger M, Benders MJNL, van Bel F, Allegaert K, Naulaers G, *et al.* Detailed statistical analysis plan for ALBINO: effect of Allopurinol in addition to hypothermia for hypoxic-ischemic Brain Injury on Neurocognitive Outcome - a blinded randomized placebo-controlled parallel group multicenter trial for superiority (phase III). *Trials*. 2024; 25: 81. <https://doi.org/10.1186/s13063-023-07828-6>.
- [60] Pang R, Meehan C, Maple G, Norris G, Campbell E, Tucker K, *et al.* Melatonin reduces brain injury following inflammation-amplified hypoxia-ischemia in a translational newborn piglet study of neonatal encephalopathy. *Journal of Pineal Research*. 2024; 76: e12962. <https://doi.org/10.1111/jpi.12962>.
- [61] Robertson NJ, Faulkner S, Fleiss B, Bainbridge A, Andorka C, Price D, *et al.* Melatonin augments hypothermic neuroprotection in a perinatal asphyxia model. *Brain: a Journal of Neurology*. 2013; 136: 90–105. <https://doi.org/10.1093/brain/awt285>.
- [62] Xue LL, Cheng J, Du RL, Luo BY, Chen L, Xiao QX, *et al.* Bone marrow mesenchymal stem cells alleviate neurological dysfunction by reducing autophagy damage via downregulation of SYNPO2 in neonatal hypoxic-ischemic encephalopathy rats. *Cell Death & Disease*. 2025; 16: 131. <https://doi.org/10.1038/s41419-025-07439-w>.
- [63] Luo BY, Zhou HS, Sun YF, Xiao QX, Chen L, She HQ, *et al.* The fate and prospects of stem cell therapy in the treatment of hypoxic-ischemic encephalopathy. *The European Journal of Neuroscience*. 2023; 58: 2384–2405. <https://doi.org/10.1111/ejn.16040>.
- [64] Linnerbauer M, Wheeler MA, Quintana FJ. Astrocyte Crosstalk in CNS Inflammation. *Neuron*. 2020; 108: 608–622. <https://doi.org/10.1016/j.neuron.2020.08.012>.
- [65] Wang C, Xue Y, Markovic T, Li H, Wang S, Zhong Y, *et al.* Blood-brain-barrier-crossing lipid nanoparticles for mRNA delivery to the central nervous system. *Nature Materials*. 2025; 24: 1653–1663. <https://doi.org/10.1038/s41563-024-02114-5>.
- [66] Kaya M, Ahishali B. Basic physiology of the blood-brain barrier in health and disease: a brief overview. *Tissue Barriers*. 2021; 9: 1840913. <https://doi.org/10.1080/21688370.2020.1840913>.
- [67] Revia RA, Stephen ZR, Zhang M. Theranostic Nanoparticles for RNA-Based Cancer Treatment. *Accounts of Chemical Research*. 2019; 52: 1496–1506. <https://doi.org/10.1021/acs.accounts.9b00101>.
- [68] Moazzam M, Zhang M, Hussain A, Yu X, Huang J, Huang Y. The landscape of nanoparticle-based siRNA delivery and therapeutic development. *Molecular Therapy: the Journal of the American Society of Gene Therapy*. 2024; 32: 284–312. <https://doi.org/10.1016/j.ymthe.2024.01.005>.
- [69] Witten J, Hu Y, Langer R, Anderson DG. Recent advances in nanoparticulate RNA delivery systems. *Proceedings of the National Academy of Sciences of the United States of America*.

- ica. 2024; 121: e2307798120. <https://doi.org/10.1073/pnas.2307798120>.
- [70] Kim H, Yuk SA, Dieterly AM, Kwon S, Park J, Meng F, *et al.* Nanosac, a Noncationic and Soft Polyphenol Nanocapsule, Enables Systemic Delivery of siRNA to Solid Tumors. *ACS Nano*. 2021; 15: 4576–4593. <https://doi.org/10.1021/acsnano.0c08694>.
- [71] Loh XJ, Lee TC, Dou Q, Deen GR. Utilising inorganic nanocarriers for gene delivery. *Biomaterials Science*. 2016; 4: 70–86. <https://doi.org/10.1039/c5bm00277j>.
- [72] Zhou Y, Han X, Jing X, Chen Y. Construction of Silica-Based Micro/Nanoplatfoms for Ultrasound Theranostic Biomedicine. *Advanced Healthcare Materials*. 2017; 6: 10.1002/adhm.201700646. <https://doi.org/10.1002/adhm.201700646>.
- [73] Huq TB, Anil Kumar Jeeja P, Dam SK, Das SS, Vivero-Escoto JL. Recent Applications of Mesoporous Silica Nanoparticles in Gene Therapy. *Advanced Healthcare Materials*. 2025; 14: e2404781. <https://doi.org/10.1002/adhm.202404781>.
- [74] Croissant JG, Fatieiev Y, Almalik A, Khashab NM. Mesoporous Silica and Organosilica Nanoparticles: Physical Chemistry, Biosafety, Delivery Strategies, and Biomedical Applications. *Advanced Healthcare Materials*. 2018; 7: 10.1002/adhm.201700831. <https://doi.org/10.1002/adhm.201700831>.
- [75] Allen TM, Cullis PR. Liposomal drug delivery systems: from concept to clinical applications. *Advanced Drug Delivery Reviews*. 2013; 65: 36–48. <https://doi.org/10.1016/j.addr.2012.09.037>.
- [76] Shah S, Dhawan V, Holm R, Nagarsenker MS, Perrie Y. Liposomes: Advancements and innovation in the manufacturing process. *Advanced Drug Delivery Reviews*. 2020; 154–155: 102–122. <https://doi.org/10.1016/j.addr.2020.07.002>.
- [77] Lu Q, Cai X, Zhang X, Li S, Song Y, Du D, *et al.* Synthetic Polymer Nanoparticles Functionalized with Different Ligands for Receptor-mediated Transcytosis across Blood-Brain Barrier. *ACS Applied Bio Materials*. 2018; 1: 1687–1694. <https://doi.org/10.1021/acsabm.8b00502>.
- [78] Dash BC, Réthoré G, Monaghan M, Fitzgerald K, Gallagher W, Pandit A. The influence of size and charge of chitosan/polyglutamic acid hollow spheres on cellular internalization, viability and blood compatibility. *Biomaterials*. 2010; 31: 8188–8197. <https://doi.org/10.1016/j.biomaterials.2010.07.067>.
- [79] Ho T, Guidolin K, Makky A, Valic M, Ding L, Bu J, *et al.* Novel Strategy to Drive the Intracellular Uptake of Lipid Nanoparticles for Photodynamic Therapy. *Angewandte Chemie (International Ed. in English)*. 2023; 62: e202218218. <https://doi.org/10.1002/anie.202218218>.
- [80] Kong W, Wei Y, Dong Z, Liu W, Zhao J, Huang Y, *et al.* Role of size, surface charge, and PEGylated lipids of lipid nanoparticles (LNPs) on intramuscular delivery of mRNA. *Journal of Nanobiotechnology*. 2024; 22: 553. <https://doi.org/10.1186/s12951-024-02812-x>.
- [81] Musyanovych A, Dausend J, Dass M, Walther P, Mailänder V, Landfester K. Criteria impacting the cellular uptake of nanoparticles: a study emphasizing polymer type and surfactant effects. *Acta Biomaterialia*. 2011; 7: 4160–4168. <https://doi.org/10.1016/j.actbio.2011.07.033>.
- [82] Khaledian S, Dayani M, Fatahian A, Fatahian R, Martinez F. Efficiency of lipid-based nano drug delivery systems in crossing the blood–brain barrier: A review. *Journal of Molecular Liquids*. 2022; 346: 118278. <https://doi.org/10.1016/j.molliq.2021.118278>.
- [83] Ross C, Taylor M, Fullwood N, Allsop D. Liposome delivery systems for the treatment of Alzheimer’s disease. *International Journal of Nanomedicine*. 2018; 13: 8507–8522. <https://doi.org/10.2147/IJN.S183117>.
- [84] Liu J, Wang T, Dong J, Lu Y. The blood-brain barriers: novel nanocarriers for central nervous system diseases. *Journal of Nanobiotechnology*. 2025; 23: 146. <https://doi.org/10.1186/s12951-025-03247-8>.
- [85] Simonis B, Vignone D, Gonzalez Paz O, Donati E, Falchetti ML, Bombelli C, *et al.* Transport of cationic liposomes in a human blood brain barrier model: Role of the stereochemistry of the gemini amphiphile on liposome biological features. *Journal of Colloid and Interface Science*. 2022; 627: 283–298. <https://doi.org/10.1016/j.jcis.2022.07.025>.
- [86] Zhu X, Tao W, Liu D, Wu J, Guo Z, Ji X, *et al.* Surface De-PEGylation Controls Nanoparticle-Mediated siRNA Delivery *In Vitro* and *In Vivo*. *Theranostics*. 2017; 7: 1990–2002. <https://doi.org/10.7150/thno.18136>.
- [87] Kim J, Eygeris Y, Gupta M, Sahay G. Self-assembled mRNA vaccines. *Advanced Drug Delivery Reviews*. 2021; 170: 83–112. <https://doi.org/10.1016/j.addr.2020.12.014>.
- [88] Meng C, Chen Z, Li G, Welte T, Shen H. Nanoplatfoms for mRNA Therapeutics. *Advanced Therapeutics*. 2021; 4: 2000099. <https://doi.org/10.1002/adtp.202000099>.
- [89] Heyes J, Hall K, Taylor V, Lenz R, MacLachlan I. Synthesis and characterization of novel poly(ethylene glycol)-lipid conjugates suitable for use in drug delivery. *Journal of Controlled Release: Official Journal of the Controlled Release Society*. 2006; 112: 280–290. <https://doi.org/10.1016/j.jconrel.2006.02.012>.
- [90] Hoet PH, Bröske-Hohlfeld I, Salata OV. Nanoparticles - known and unknown health risks. *Journal of Nanobiotechnology*. 2004; 2: 12. <https://doi.org/10.1186/1477-3155-2-12>.
- [91] Zamanian JL, Xu L, Foo LC, Nouri N, Zhou L, Giffard RG, *et al.* Genomic analysis of reactive astrogliosis. *The Journal of Neuroscience: the Official Journal of the Society for Neuroscience*. 2012; 32: 6391–6410. <https://doi.org/10.1523/JNEUROSCI.6221-11.2012>.
- [92] Li X, Zhao H, Tan X, Kostrzewa RM, Du G, Chen Y, *et al.* Inhibition of connexin43 improves functional recovery after ischemic brain injury in neonatal rats. *Glia*. 2015; 63: 1553–1567. <https://doi.org/10.1002/glia.22826>.
- [93] Chen X, Sadowska GB, Zhang J, Kim JE, Cummings EE, Bodge CA, *et al.* Neutralizing anti-interleukin-1 β antibodies modulate fetal blood-brain barrier function after ischemia. *Neurobiology of Disease*. 2015; 73: 118–129. <https://doi.org/10.1016/j.nbd.2014.09.007>.
- [94] Yang J, Dong J, Li H, Gong Z, Wang B, Du K, *et al.* Circular RNA HIPK2 Promotes A1 Astrocyte Activation after Spinal Cord Injury through Autophagy and Endoplasmic Reticulum Stress by Modulating miR-124-3p-Mediated Smad2 Repression. *ACS Omega*. 2023; 9: 781–797. <https://doi.org/10.1021/acsomega.3c06679>.
- [95] Rice JE, 3rd, Vannucci RC, Brierley JB. The influence of immaturity on hypoxic-ischemic brain damage in the rat. *Annals of Neurology*. 1981; 9: 131–141. <https://doi.org/10.1002/ana.410090206>.
- [96] Zhang LQ, Gao SJ, Sun J, Li DY, Wu JY, Song FH, *et al.* DKK3 ameliorates neuropathic pain via inhibiting ASK-1/JNK/p-38-mediated microglia polarization and neuroinflammation. *Journal of Neuroinflammation*. 2022; 19: 129. <https://doi.org/10.1186/s12974-022-02495-x>.
- [97] Pan W, Banks WA, Fasold MB, Bluth J, Kastin AJ. Transport of brain-derived neurotrophic factor across the blood-brain barrier. *Neuropharmacology*. 1998; 37: 1553–1561. [https://doi.org/10.1016/s0028-3908\(98\)00141-5](https://doi.org/10.1016/s0028-3908(98)00141-5).
- [98] Hossmann KA. Experimentelle Grundlagen der Ischämietoleranz des Hirns [Experimental principles of tolerance of the brain to ischemia]. *Z Kardiol*. 1987; 76 Suppl 4:47–66. <https://pubmed.ncbi.nlm.nih.gov/3327266>.

- [99] Nalivaeva NN, Rybnikova EA. Editorial: Brain Hypoxia and Ischemia: New Insights Into Neurodegeneration and Neuroprotection. *Frontiers in Neuroscience*. 2019; 13: 770. <https://doi.org/10.3389/fnins.2019.00770>.
- [100] Liu Q, Zhou S, Wang X, Gu C, Guo Q, Li X, *et al*. Apelin alleviated neuroinflammation and promoted endogenous neural stem cell proliferation and differentiation after spinal cord injury in rats. *Journal of Neuroinflammation*. 2022; 19: 160. <https://doi.org/10.1186/s12974-022-02518-7>.
- [101] Gidday JM. Cerebral preconditioning and ischaemic tolerance. *Nature Reviews. Neuroscience*. 2006; 7: 437–448. <https://doi.org/10.1038/nrn1927>.
- [102] Sun L, Han R, Guo F, Chen H, Wang W, Chen Z, *et al*. Antagonistic effects of IL-17 and Astragaloside IV on cortical neurogenesis and cognitive behavior after stroke in adult mice through Akt/GSK-3 β pathway. *Cell Death Discovery*. 2020; 6: 74. <https://doi.org/10.1038/s41420-020-00298-8>.